First-principles calculations of hyperfine parameters with the all-electron mixed-basis method

M. S. Bahramy, M. H. F. Sluiter,* and Y. Kawazoe
Institute for Materials Research, Tohoku University, Sendai 980-8577, Japan
(Received 17 September 2005; revised manuscript received 23 November 2005; published 13 January 2006)

Within density functional theory, an efficient and accurate method for calculating and analyzing hyperfine parameters has been developed. The so-called mixed-basis method expands the one-electron wave functions in terms of both localized nucleus-centered functions and plane waves and thereby affords an accurate representation for the spin density both in the immediate vicinity of the nucleus and in the bonding regions. The current method is compared with experiment and the best computational methods reported in the literature. The mixed-basis approach is shown to yield highly accurate isotropic and anisotropic hyperfine parameters with modest computational effort. The atom-centered radial representation of the potentials and spin densities allows us to analyze, within the context of density functional theory, the effect of the exchange interaction on the individual core levels in a physically transparent way.

DOI: 10.1103/PhysRevB.73.045111 PACS number(s): 71.70.−d, 71.15.Ap, 32.10.Fn

I. INTRODUCTION

Determination of the geometry of clusters and the identification of pointlike defects in crystals heavily rely on the matching of hyperfine parameters (HFP's) as determined from experiment and as computed from atomic models.[1–6] Simply put, atomic models that give rise to HFP's that agree well with experimental values are deemed to be realistic. The accurate computation of HFP's is therefore of considerable utility and interest. The increasing efforts in the area of nanoscience and nanotechnology, such as for the development of nanomagnets,[7] quantum dots,[8] and nanocrystals,[9] further contribute to the importance of hyperfine studies. Among the challenges in performing such calculations within the context of density functional theory one can mention (1) the accurate representation of, the spin density at, and in the vicinity of, the nucleus, (2) the proper treatment of relativistic effects, (3) the proper treatment of the strong charge density gradients in the nucleus region, and (4) the self-interaction correction. Recently, there has been an emphasis on challenges (2),[10–13] (3),[14,15] and (4).[16] However, as is known from other studies, a good representation of the wave functions is often paramount; e.g., consider the many studies of the weakly bonded Be dimer.[17,18]

In this paper, we shall focus on the first challenge. The importance of accurately representing the spin density near the nucleus is apparent right away from the fact that (1) the Fermi contact interaction (also referred to as an isotropic HFP) is proportional to the spin density at the nucleus and (2) that the nonisotropic part of the hyperfine interaction is proportional to the volume integral over the spin density divided by the distance to the nucleus to the third power.

Although pseudopotential treatments for the calculation of the hyperfine tensor have been developed,[19,20] here we adopt an all-electron formalism because it treats the spin polarization of the core states implicitly. As we are interested in the anisotropic part of the hyperfine tensor, we do not make shape approximations to the charge density or to the potential. Among the so-called all-electron full-potential methods, the mixed-basis (MB) method is conceptually if not computationally perhaps the most appealing.[21] In the MB method, the electronic eigenstates are expressed in terms of confined atomic eigenfunctions (atomic orbitals from now on) supplemented with plane waves. The atomic orbitals provide a good approximation for the core states, whereas the plane waves are computationally expedient and are needed only to describe the deviation of the actual eigenstates from those in the atomic configuration. For that reason, elements in the first row of the periodic table, as well as transition metals, are rather well described with relatively few plane waves only.[22,23]

It is important to point out that the radial part of an atomic orbital is represented as a numerical function. Therefore at the nucleus, unlike say, a Gaussian, there is no restraint on the value of the first derivative and unlike other functional forms there is no constraining relation between function value and derivative. The atomic orbitals are confined within nonoverlapping atomic spheres, avoiding time-consuming overlap integrals between radial functions on adjacent nuclei and greatly facilitating the accurate calculation of forces. Furthermore, the matrix elements between plane waves, which are the largest part in the Hamiltonian matrix, do not need to be stored in computer memory just as in the case of the standard plane-wave approaches. Hence, compared to other full-potential all-electron methods the MB approach can be expected to be conceptually and computationally advantageous. The calculation of forces is of importance because relaxation of atomic positions is known to be a significant factor for the accurate calculation of HFP's.[24] Here, the density functional theory is used in the local spin density formalism only because a previous study has shown that improvements in the HFP's resulting from including gradient terms are very minor.[14] The MB approach was originally introduced within the pseudopotential formalism for the accurate treatment of transition metals.[22,23,25–27] Therefore, we describe how we extended the MB approach to an all-electron formalism. Next, the method is applied to some small clusters for which experimental data are available and for which other theoretical results have been reported and the MB results are examined and compared.

II. FORMULATION

The characteristic feature of the all-electron MB approach is that the Kohn-Sham[28] wave functions are expanded by a MB, which consists of plane waves (PW's) and a Bloch sum of well-localized functions centered at atomic nuclei $\mathbf{R}_j$, the so-called atomic orbitals (AO's),

$$\Psi^{\lambda}(\mathbf{r}) = \sum_{\mathbf{G}} c_{\mathbf{G}}^{\lambda} \frac{e^{i\mathbf{G}\cdot\mathbf{r}}}{\sqrt{\Omega}} + \sum_{j}\sum_{nlm} c_{jnlm}^{\lambda}\Phi_{jnlm}(\mathbf{r}-\mathbf{R_j}) = \sum_{\mathbf{G}} c_{\mathbf{G}}^{\lambda}|\mathbf{G}\rangle + \sum_{j}\sum_{nlm} c_{jnlm}^{\lambda}|\Phi_{jnlm}\rangle = \sum_{\xi} c_{\xi}^{\lambda}|\Xi_{\xi}\rangle, \quad (1)$$

where the superscript λ is the index of a Kohn-Sham eigenstate, the boldfaced $\mathbf{r}(\mathbf{G})$ indicates a vector in direct (reciprocal) space, Ω is the volume of the unit cell, c is the expansion coefficient, and Φ denotes the AO. The subscripts n, l, and m refer to the principal, angular momentum, and magnetic quantum numbers, respectively. In the second equality, the basis functions $\Xi_{\xi}(\mathbf{r})$ refer to either PW or AO basis functions and c_{ξ}^{λ} denotes the coefficient of the ξ basis function in the λ Kohn-Sham eigenstate. Since the PW's and AO's are not orthogonal to each other, the generalized eigenvalue equation $\Sigma_{\xi'} H_{\xi\xi'} c_{\xi'}^{\lambda} = \epsilon^{\lambda}\Sigma_{\xi'} S_{\xi\xi'} c_{\xi'}^{\lambda}$ must be solved to determine the Kohn-Sham energy eigenvalues ϵ^{λ}, where $H_{\xi\xi'} = \langle\Xi_{\xi}|H|\Xi_{\xi'}\rangle$ and $S_{\xi\xi'} = \langle\Xi_{\xi}|\Xi_{\xi'}\rangle$ denote the Hamiltonian and overlap matrix elements between basis functions ξ and ξ'. In matrix form, the generalized eigenvalue equation can be written as $H\Psi^{\lambda} = \epsilon^{\lambda} S\Psi^{\lambda}$, where Ψ^{λ} is a column vector whose elements are given by $c_{\nu,\xi}$. This generalized eigenvalue problem can be transformed to a standard eigenvalue problem by a conventional Cholesky decomposition.[25]

A. Basis functions

Each AO is confined within a nonoverlapping atomic sphere of radius r_c, referred to as the cutoff radius. The AO's are of the form

$$\Phi_{jnlm}(\mathbf{r}_j) = R_{jnl}(|\mathbf{r}_j|) Y_l^m(\theta,\phi), \quad (2)$$

where Y refers to a spherical harmonic. Cartesian vectors, here and below, are indicated in boldface. The positional vector relative to the nucleus is given by $\mathbf{r}_j = \mathbf{r} - \mathbf{R}_j$, and the radial coordinate is $r_j = |\mathbf{r} - \mathbf{R}_j|$. The radial part of the AO, $R_{jnl}(r_j)$, is stored numerically on a logarithmic radial mesh r_j from the vicinity of the nucleus $\mathbf{R}_j$ to the cutoff radius $r_{c,j}$. Similarly, all other spherically symmetric functions such as the AO-related spherical electron density and the spherical potential for AO's (see below) are stored on the same logarithmic mesh along the radial coordinate. Here and below, wherever no confusion is possible, we omit the subscript j in $\mathbf{r}_j$, r_j, and $r_{c,j}$ for brevity. For properties X associated with atomic spheres j the following notation has been adopted:

$$X(\mathbf{r}) = \sum_{j} X(\mathbf{R}_j + \mathbf{r}_j), \quad (3)$$

with

$$X(\mathbf{R}_j + \mathbf{r}_j) = X_j(\mathbf{r}_j), \quad (4)$$

where X_j is understood to be associated exclusively with sphere j.

It should be noted that the PW's are used globally unlike, say, the full-potential linearized angmented plane-wave (FLAPW) method[29] where PW's are used in the interstitial regions only. This simplifies the MB formalism considerably because there is no need for matching at the atomic sphere boundary. Instead, we must assure that the wave functions and charge densities are smooth at the edge of the atomic spheres. Therefore, we require that the AO's vanish and also have a vanishing first derivative at the sphere edge. This means that the radial part satisfies

$$R_{jnl}(r_c) = 0, \quad \left(\frac{\partial R_{jnl}(r)}{\partial r}\right)_{r=r_c} = 0. \quad (5)$$

To assure that core states are well represented the functions $R_{jnl}(r)$ are derived from an atomic calculation. Initially, a Herman-Skillman-type calculation is performed for an isolated atom which provides atomic radial wave functions $P_{jnl}(r)$. For brevity and without loss of generality, we absorb the r^l term in $P_{jnl}(r)$. The functions P do not generally satisfy Eq. (5). Therefore, low-order polynomials of r, which do not destroy the properties of the radial functions near $r=0$, are subtracted from P such that Eq. (5) holds,

$$\tilde{R}_{jnl}(r) = \begin{cases} P_{jnl}(r) - a_{00} - a_{02}r^2, & l=0, \\ P_{jnl}(r) - a_{11}r - a_{12}r^2, & l=1, \\ P_{jnl}(r) - a_{22}r^2 - a_{23}r^3, & l=2, \\ P_{jnl}(r) - a_{33}r^3 - a_{34}r^4, & l=3, \end{cases} \quad (6)$$

with

$$a_{00} = P_{jn0}(r_c) - a_{02}r_c^{\,2}, \quad a_{02} = r_c^{\,-1}\frac{1}{2}\frac{\partial P_{jn0}}{\partial r}(r_c),$$

$$a_{11} = r_c^{-1}P_{jn1}(r_c) - a_{12}r_c, \quad a_{12} = r_c^{\,-2}\left(r_c\frac{\partial P_{jn1}}{\partial r}(r_c) - P_{jn1}(r_c)\right),$$

$$a_{22} = r_c^{\,-2}P_{jn2}(r_c) - a_{23}r_c,$$

$$a_{23} = r_c^{\,-3}\left(r_c\frac{\partial P_{jn2}}{\partial r}(r_c) - 2P_{jn2}(r_c)\right),$$

$$a_{33} = r_c^{\,-3}P_{jn3}(r_c) - a_{34}r_c,$$

$$a_{34} = r_c^{\,-4}\left(r_c\frac{\partial P_{jn3}}{\partial r}(r_c) - 3P_{jn3}(r_c)\right). \quad (7)$$

This truncation procedure is illustrated in Fig. 1. A consequence of truncating and subtracting polynomials from P is that the functions $\tilde{R}_{jnl}$ and $\tilde{R}_{jn'l}$ are no longer orthogonal. The functions $\tilde{R}$ are orthogonalized with

$$R_{jnl}(r) = \tilde{R}_{jnl}(r) - \sum_{n'<n} R_{jn'l}(r) \int_0^{r_c} dx 4\pi r^2 \tilde{R}_{jnl}(x) R_{jn'l}(x). \tag{8}$$

Particularly in the case of outer valence states it sometimes happens that the remaining charge in a radial function R thus calculated is exceedingly small. Then, it does not much improve the description of the wave functions and an alternate method for obtaining $\tilde{R}$ from P is used. Instead of subtracting a polynomial, we multiply by a function:[30] $\tilde{R}_{jnl}(r) = P_{jnl}(r)M(r)$, where $M(r)$ is defined as

$$M(r) = \begin{cases} 1, & r \leqslant r_c - \Delta r, \\ 1 - 3\left(\dfrac{r + \Delta r - r_c}{\Delta r}\right)^2 + 2\left(\dfrac{r + \Delta r - r_c}{\Delta r}\right)^3, & r > r_c - \Delta r, \quad r < r_c, \\ 0, & r \geqslant r_c, \end{cases} \tag{9}$$

where Δr is the width over which the radial wave function is modified, typically set to about $r_c/2$. In this scheme, more of the original charge is retained so that the basis function $R_{jnl}(r)$ contributes more to an improved description of the wave functions. However, if still too little charge remains, the AO is removed from the basis set. After orthogonalization, the $R_{jnl}(r)$ are normalized to unity as a final step, so that

$$\langle \Phi_{jnlm} | \Phi_{j'n'l'm'} \rangle = \delta_{jj'} \delta_{nn'} \delta_{ll'} \delta_{mm'}. \tag{10}$$

Now that the final form of the AO has been determined, there is still an important issue that needs to be addressed: overcompleteness of the basis for the Kohn-Sham wave functions. This is detailed in the section on the overlap matrix below.

B. Overlap matrix

Since the PW's form an orthonormal set and the AO's have been orthonormalized as described above, elements between PW's and AO's only are of interest. The $\langle \Phi_{jnlm} | G \rangle$ elements are calculated in real space as set forth by Elsässer *et al.*[27] by locally expanding the plane waves,

$$e^{i\mathbf{G}\cdot\mathbf{r}} = e^{i\mathbf{G}\cdot\mathbf{r}_j} e^{i\mathbf{G}\cdot\mathbf{R}_j} = e^{i\mathbf{G}\cdot\mathbf{R}_j} \sum_{L=0}^{\infty} \sum_{M=-L}^{+L} 4\pi i^L j_L(Gr_j) Y_L^M(\hat{G}) Y_L^M(\hat{r}_j), \tag{11}$$

where j_L is a spherical Bessel function of the first kind of order L and the solid angles $\hat{r}_j = \mathbf{r}_j/|\mathbf{r}_j|$ and $\hat{G} = \mathbf{G}/|\mathbf{G}|$ are indicated with a caret. Then, by substitution of Eqs. (2) and (11), the overlap can be written as

$$\langle \Phi_{jnlm} | \mathbf{G} \rangle = S_{jnlm\mathbf{G}} = \frac{i^l}{\sqrt{\Omega}} e^{i\mathbf{G}\cdot\mathbf{R}_j} Y_l^m(\hat{G}) \int_0^{r_c} dr_j 4\pi r_j^2 R_{jnl}(r_j) j_l(Gr_j). \tag{12}$$

In order for the diagonalization of the Hamiltonian to be numerically stable, the overlap matrix must be positive definite and not nearly singular. In the MB approach nearly singular overlap matrices can occur when an AO is well represented by a combination of PW's. Then, the basis is said to be "overcomplete." Therefore, when for any AO the norm after orthogonalization with respect to the PW's according to

$$|\Phi_{jnlm}^{orth:PW}\rangle = |\Phi_{jnlm}\rangle - \sum_{\mathbf{G}} |\mathbf{G}\rangle\langle\mathbf{G}|\Phi_{jnlm}\rangle \tag{13}$$

is less than some small value, that AO is discarded from the basis set. Naturally, whether a particular AO is discarded depends on the cutoff energy for the PW's. As the PW's and AO's each form orthonormal sets by construction [see Eq. (10)], this simple procedure avoids numerical instability due to overcompleteness in the wave-function basis.

C. Hamiltonian

According to density functional theory[28,31,32] (DFT) in the local density approximation (LDA), one may derive the Kohn-Sham Hamiltonian as

$$H = -\frac{1}{2}\nabla^2 + V_H(\mathbf{r}) + V_N(\mathbf{r}) + V_{xc}(\mathbf{r}), \tag{14}$$

where the first term is the electron kinetic energy. V_H, V_N, and $V_{xc}(\mathbf{r})$ represent, respectively, the Hartree potential, the

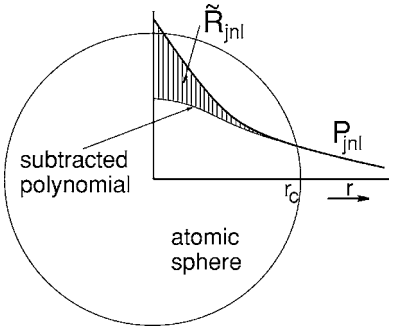

FIG. 1. Construction of AO's from atomic radial wave functions.

nucleus Coulomb potential, and the exchange-correlation potential,

$$V_H(\mathbf{r}) = \int d\mathbf{r}' \frac{\rho(\mathbf{r}')}{|\mathbf{r}-\mathbf{r}'|}, \quad V_N(\mathbf{r}) = -\sum_j \frac{Z_j}{|\mathbf{r}-\mathbf{R_j}|},$$

$$V_{xc}(\mathbf{r}) = \frac{\partial E_{xc}[\rho]}{\partial \rho(\mathbf{r})}, \tag{15}$$

where Z_j is the atomic number, $\rho(\mathbf{r})$ is the electron density, and $E_{xc}[\rho]$ is the exchange-correlation energy which is a functional of $\rho(\mathbf{r})$. The local spin density approximation (LSDA) of DFT is analogous. Likewise the generalized gradient approximation (GGA) of the DFT affects the details concerning the definition of $E_{xc}[\rho]$ only. Three types of Hamiltonian matrix elements must be distinguished: $\langle G|H|G'\rangle$, $\langle G|H|\Phi\rangle$, and $\langle \Phi|H|\Phi'\rangle$. These elements are computed while taking advantage of the global and radial representations as will be detailed below.

D. Electron density

The electron density $\rho(\mathbf{r})$ can be decomposed into plane-wave and atomic orbital contributions as follows:

$$\rho(\mathbf{r}) = \rho^{PW\ PW}(\mathbf{r}) + \sum_j \rho_j^{AO\ AO}(\mathbf{r}) + \sum_j \rho_j^{PW\ AO}(\mathbf{r}). \tag{16}$$

These contributions are computed with

$$\rho^{PW\ PW}(\mathbf{r}) = \frac{2}{\Omega}\sum_\lambda f^\lambda \sum_{\mathbf{G}} \sum_{\mathbf{G}'} c_{\mathbf{G}'}^{\lambda *} c_{\mathbf{G}}^{\lambda} e^{i(\mathbf{G}-\mathbf{G}')\cdot\mathbf{r}}, \tag{17}$$

$$\rho_j^{PW\ AO}(\mathbf{r}) = \frac{2}{\sqrt{\Omega}}\sum_\lambda f^\lambda \sum_{\mathbf{G}} \sum_{nlm} c_{\mathbf{G}}^{\lambda *} c_{jnlm}^{\lambda} e^{-i\mathbf{G}\cdot\mathbf{r}} \Phi_{jnlm}(\mathbf{r}) + \text{c.c.}, \tag{18}$$

$$\rho_j^{AO\ AO}(\mathbf{r}) = 2\sum_\lambda f^\lambda \sum_{nlm} \sum_{n'l'm'} c_{jn'l'm'}^{\lambda *} c_{jnlm}^{\lambda} \Phi_{jn'l'm'}^{*}(\mathbf{r}) \Phi_{jnlm}(\mathbf{r}), \tag{19}$$

where the prefactor of 2 accounts for spin duplicity. f^λ is the occupancy of level λ, computed with the Fermi-Dirac distribution function through

$$f^\lambda = [1 + e^{(\epsilon^\lambda - \epsilon_F)/k_B T^e}]^{-1}, \tag{20}$$

where ϵ^λ is the corresponding eigenvalue of the Hamiltonian, ϵ_F is the Fermi energy, k_B is the Boltzmann constant, and T^e denotes the electron temperature.

The PWPW contribution [Eq. (17)] is computed quickly in reciprocal space for small numbers of plane waves only. When the number of plane waves is large a more efficient real-space method is used:

$$\rho^{PW\ PW}(\mathbf{r}) = 2\sum_\lambda f^\lambda c^{\lambda *}(\mathbf{r}) c^\lambda(\mathbf{r}), \tag{21}$$

where the coefficients $c^\lambda(\mathbf{r})$ are the Fourier transform of $c_{\mathbf{G}}^\lambda$. The AO-related contributions have nonzero values within the atomic spheres only. The angular components of $\rho_j^{PW\ AO}$ and $\rho_j^{AO\ AO}$ are conveniently computed through a projection onto spherical harmonics,

$$\rho_{j,LM}(r_j) = \int d\hat{r} Y_L^{M*}(\hat{r}_j) \rho_j(\mathbf{r}_j), \tag{22}$$

which gives, after substitution with Eqs. (2) and (11),

$$\rho_{j,LM}^{PW\ AO}(r_j) = \frac{16\pi}{\sqrt{\Omega}} \text{Re}\left[\sum_{\mathbf{G}} \sum_{nlm,l'm'} i^{l'} j_{l'}(Gr_j) Y_{l'}^{m'*}(\hat{G}) e^{i\mathbf{G}\cdot\mathbf{R}_j} \times R_{jnl}(r_j) C_{LM,l'm',lm} \sum_\lambda f^\lambda c_{jnlm}^{\lambda *} c_{\mathbf{G}}^{\lambda} \right], \tag{23}$$

$$\rho_{j,LM}^{AO\ AO}(r_j) = 2 \sum_{nlm,n'l'm'} R_{jnl}(r_j) R_{jn'l'}(r_j) C_{l'm',LM,lm} \sum_\lambda f^\lambda c_{jnlm}^{\lambda *} c_{jn'l'm'}^{\lambda}, \tag{24}$$

where "Re" indicates the real part and $C_{l'm',LM,lm}$ is a Gaunt coefficient defined as $C_{l'm',LM,lm} = \int d\hat{r} Y_{l'}^{m'*} Y_L^M Y_l^m$.[33,34] The Gaunt coefficients are real and vanish unless the triangle condition is satisfied: $m' = M - m$ and $|l'| \leqslant |L-l|$.[35] The spherical averages are then trivially computed through the $L=0$ components, using $C_{lm,00,l-m} = 1/\sqrt{4\pi}$,

$$\rho_{j,L=0}^{PW\ AO}(r_j) = 8\sqrt{\frac{\pi}{\Omega}} \text{Re}\left[\sum_{\mathbf{G}} \sum_{nlm} i^l j_l(Gr_j) Y_l^m(\hat{G}) e^{i\mathbf{G}\cdot\mathbf{R}_j} \times R_{jnl}(r_j) \sum_\lambda f^\lambda c_{jnlm}^{\lambda *} c_{\mathbf{G}}^{\lambda} \right], \tag{25}$$

$$\rho_{j,L=0}^{AO\ AO}(r_j) = \frac{1}{\sqrt{\pi}} \sum_{nlm,n'} R_{jn'l}(r_j) R_{jnl}(r_j) \sum_\lambda f^\lambda c_{jn'lm}^{\lambda *} c_{jnlm}^{\lambda}. \tag{26}$$

The spherically averaged charge density centered at atom j,

$$\rho_j^{radial}(r_j) = [\rho_{j,L=0}^{PW\ AO}(r_j) + \rho_{j,L=0}^{AO\ AO}(r_j)] Y_0^0(\hat{r}_j) = \frac{1}{\sqrt{4\pi}} [\rho_{j,L=0}^{PW\ AO}(r_j) + \rho_{j,L=0}^{AO\ AO}(r_j)], \tag{27}$$

combined with the PW-PW contribution on the global mesh gives in many cases an adequate description of the charge density. However, when there is significant covalent bonding the nonspherical part of the PW-AO and AO-AO charge density may be important. These $L \geqslant 1$ terms in Eqs. (23) and (24) can be easily computed and are added to the charge density on the global mesh:

$$\rho^{global}(\mathbf{r}) = \rho^{PW\ PW}(\mathbf{r}) + \sum_{L\geq 1,M}\sum_{j} Y_L^M(\hat{r}_j) \times [\rho_{j,LM}^{AO\ AO}(r_j) + \rho_{j,LM}^{PW\ AO}(r_j)]. \quad (28)$$

The charge density thus is divided into a global and a radial part:

$$\rho(\mathbf{r}) = \rho^{global}(\mathbf{r}) + \sum_j \rho_j^{radial}(\mathbf{r}_j). \quad (29)$$

An alternate method of computing $\rho_j^{PW\ AO}$ directly on the global mesh through projecting the AO's onto PW's with

$$\rho^{PW\ AO}(\mathbf{G}-\mathbf{G}') = 2\sum_{jnlm}\sum_{\mathbf{G}'} \mathrm{Re}\left[\langle \mathbf{G}|\Phi_{jnlm}\rangle \sum_{\lambda} f^{\lambda} c_{\mathbf{G}'}^{\lambda\,*} c_{jnlm}^{\lambda}\right] \quad (30)$$

does not strictly satisfy the condition that $\rho^{PW\ AO}$ be zero outside the atomic spheres and is generally insufficiently accurate.

The total charge density can be represented on either the global mesh or, within the atomic spheres on the radial mesh, with

$$\rho_{tot}^{global}(\mathbf{G}) = \rho^{global}(\mathbf{G}) + \rho^{radial}(G), \quad (31)$$

with the spherically Fourier-transformed radial charge density,

$$\rho^{radial}(G) = \sum_j e^{i\mathbf{G}\cdot\mathbf{R}_j} \int_0^{r_c} dr_j 4\pi r_j^2 j_0(Gr_j)\rho_j^{radial}(r_j), \quad (32)$$

$$\rho_{tot}^{radial}(r_j) = \rho_j^{radial}(r_j) + \frac{1}{2\pi G_{max}} \times \int_0^{G_{max}} dG G^2 j_0(Gr) \int d\hat{G} e^{-i\mathbf{G}\cdot\mathbf{R}_j}\rho^{global}(\mathbf{G}). \quad (33)$$

Of course, the radial representation of ρ_{tot} is spherically averaged and therefore approximate. The global representation in reciprocal space requires a very high cutoff energy for the Fourier transform of the radial part due to the highly localized core states. Therefore, in the calculation of the exchange-correlation potential a direct-space method is used where the radial charge density is sampled at points r_j which correspond to the global mesh points $\mathbf{r}$ with

$$\rho_{tot}^{global}(\mathbf{r}) = \rho^{global}(\mathbf{r}) + \sum_j \rho_j^{radial}(r_j). \quad (34)$$

This gives "exact" values for ρ_{tot}^{global} on the mesh points $\mathbf{r}$.

E. Potential

In the MB the potential is expressed as the sum of two parts, a global part and a radial part within each of the atomic spheres. The exchange-correlation potential V_{xc} is a function of the total charge density and as such requires a careful summation of global and spherical charge densities as in Eqs. (34) and (33). Moreover, we seek to express V_{xc} as the sum of a spherically averaged potential $V_{xc}^{radial}(|\mathbf{r}_j|)$ inside atomic spheres and a global term $V_{xc}^{global}(\mathbf{r})$ as in Eq. (29). The spherically averaged potential is indispensable because the global term cannot represent accurately the rapid variation near the atomic cores.

Implementing the generalized gradient approximation in the MB method is more complicated than in pseudopotential methods because in the former the *total* charge density must be considered which nearly diverges in the vicinity of the nuclei. In the GGA the Laplacian must be evaluated which is even more nearly divergent than the total charge density itself,[36] while there is a nonanalyticity at the nucleus which can be remedied with, e.g., a finite nucleus model.[14] Fortunately, on the global mesh the evaluation of the Laplacian can be circumvented through the method of White and Bird.[37] On the radial mesh, however, the near divergence of the Laplacian remains. The solution to this problem implemented within the MB is to represent the total charge density of the global mesh, using a very high cutoff for the **G** vectors, and employing the White- Bird method. Then, the radial components of the exchange-correlation potential and energy density are extracted by means of a radial Fourier transform. Within the context of hyperfine calculations, the work by Battocletti *et al.*[14] indicates that the "finite-nucleus model +GGA" does not produce significant improvement over the L(S)DA, however. Therefore, it maybe most practical to optimize the atomic positions with a pseudopotential or PAW method while performing the hyperfine calculations with an all-electron LSDA method such as the MB method presented here.

In the case of the LDA a more accurate method can be adapted as follows. First, the total charge density is calculated in real space on the global mesh with Eq. (34), which gives $V_{xc,tot}^{global}(\mathbf{r})$ by applying an appropriate functional.[38] Next, the spherically averaged total charge density is computed within each of the atomic spheres [Eq. (33)] which provides $V_{xc,tot}^{radial}(r_j)$. The latter is discontinuous at $r_j = r_c$ because the total charge density does not vanish near the edge of the sphere. This is remedied by subtracting a parabola, in the same manner as the *s*-like atomic radial wave functions were made to vanish smoothly at $r = r_c$,

$$V_{xc}^{radial}(r_j) = V_{xc,tot}^{radial}(r_j) - V_{xc,tot}^{radial}(r_c) + \frac{r_c^2 - r^2}{2r_c}\left(\frac{\partial V_{xc,tot}^{radial}}{\partial r}\right)_{r=r_c}. \quad (35)$$

Finally, a smoothly varying global part of the exchange-correlation potential is obtained with

$$V_{xc}^{global}(\mathbf{r}) = V_{xc,tot}^{global}(\mathbf{r}) - \sum_j V_{xc}^{radial}(r_j). \quad (36)$$

As in the case of the charge density [see Eq. (29)] and exchange-correlation potential, the Hartree potential is represented as the sum of a global part and radial parts. The global part $V_H^{global}(\mathbf{r})$ is computed through

$$V_H^{global}(\mathbf{G}) = 4\pi\rho^{global}(\mathbf{G})/G^2 \tag{37}$$

or, in case the Coulomb potentials are truncated (see below), through

$$V_H^{global}(\mathbf{G}) = 4\pi\rho^{global}(\mathbf{G})[1-\cos(Gr_t)]/G^2, \tag{38}$$

where r_t is the truncation radius. When the Hartree potential is not truncated the $\mathbf{G}=\mathbf{0}$ term is divergent. However, for charge-neutral systems it cancels with the corresponding nucleus potential term as will be discussed below [see Eqs. (48) and (49)].

The Hartree potential that derives from the radial charge density is obtained in a general form using the multipole expansion,

$$V_{H,jlm}^{AO}(r_j) = \frac{4\pi}{(2l+1)r_j^{l+1}}\int_0^{r_j}\rho_{jlm}^{AO}(r)r^{l+2}dr + \frac{4\pi r_j^l}{2l+1}\int_{r_j}\rho_{jlm}^{AO}(r)r^{1-l}dr, \tag{39}$$

where $\rho_{jlm}^{AO}=\rho_{jlm}^{PW\ AO}+\rho_{jlm}^{AO\ AO}$, which are given by Eqs. (23) and (24). Retaining the $l=0$ contribution only and dividing in a short-ranged part $V_{H,j}^{radial}(r_j)$ within the atomic sphere and a long-ranged part $V_{H\text{-}long,j}^{radial}(r_j)$ that extends beyond the atomic sphere gives

$$V_{H,j}^{radial}(r_j) = \frac{4\pi}{r_j}\int_0^{r_j}\rho_j^{radial}(r)r^2dr + 4\pi\int_{r_j}^{r_c}\rho_j^{radial}(r)rdr \quad \text{for } r_j \leqslant r_c, \tag{40}$$

$$V_{H\text{-}long,j}^{radial}(r_j) = \frac{4\pi}{r_j}\int_0^{r_c}\rho_j^{radial}(r)r^2dr \quad \text{for } r_j \geqslant r_c. \tag{41}$$

$V_{H,j}^{radial}$ is solved with a numerical integration on the radial mesh using Simpson's method while $V_{H\text{-}long,j}^{radial}$ is integrated analytically, leading to

$$V_{H\text{-}long,j}^{radial}(r_j) = \frac{Q_j}{r_j} \quad \text{with } Q_j = \int_0^{r_c}4\pi r^2\rho_j^{radial}(r)dr, \tag{42}$$

where Q_j is the electronic charge on the radial mesh inside the atomic sphere centered on atom j. Note that $V_{H,j}^{radial}$ is defined only within atomic sphere j, whereas $V_{H\text{-}long,j}^{radial}$ is defined only outside sphere j. $V_{H\text{-}long,j}^{radial}$ is never explicitly calculated; rather, it is absorbed in the long-ranged nucleus potential [see Eq. (44)].

The nucleus potential, also, is written as the sum of two parts, a smooth long-ranged potential $V_{N,j}^{global}(\mathbf{r})$ on the global mesh and a highly localized potential within the atomic spheres $V_{N,j}^{radial}(r_j)$ where

$$V_N(\mathbf{r}) = -\sum_j\frac{Z_j}{|\mathbf{r}-\mathbf{R_j}|} = V_{N\text{-}bare}^{global}(\mathbf{r}) + \sum_j V_{N,j}^{radial}(r_j). \tag{43}$$

The long-ranged bare nucleus potential has the same form as the long-ranged radial Hartree potential, so that they can be combined to give the long-ranged screened nucleus potential

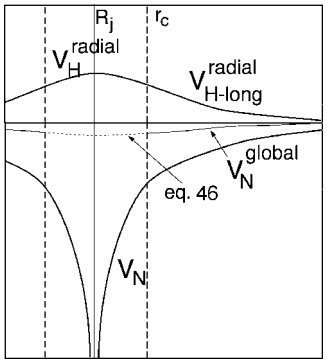

FIG. 2. Definition of screened global nucleus potential.

$$V_N^{global}(\mathbf{r}) = V_{N\text{-}bare}^{global}(\mathbf{r}) + \sum_j V_{H\text{-}long,j}^{radial}(r_j) = -\sum_j\frac{Z_j-Q_j}{|\mathbf{r}-\mathbf{R_j}|} = -\sum_j\frac{Z_j^s}{|\mathbf{r}-\mathbf{R_j}|} \quad \text{for } r_j \geqslant r_c, \tag{44}$$

where $Z_j^s=Z_j-Q_j$ is the screened nuclear charge. The long tail of the nucleus potential can optionally be truncated in real space to eliminate interactions with neighboring clusters (unit cells) with

$$V_{N,j}^{global}(\mathbf{r}_j) = 0 \quad \text{for } r_j \geqslant r_t, \tag{45}$$

where r_t is typically set to a quarter of the edge of the (cubic) unit cell. From now on, references to the global nucleus potential shall refer to the screened nucleus unless explicitly stated otherwise. So far, the global nucleus potential has not been defined within the atomic sphere from which it originates. For this part we are at liberty to select any radial function, provided that it is subtracted from the radial part of the nucleus potential so that within the spheres the global and radial parts add up to Z_j/r_j [see also Eq. (43)]. Naturally, a smooth radial function is selected that can be well represented with a small number of plane waves only. Therefore, continuity of the potential and its derivative are imposed at the sphere boundary using a low-order polynomial

$$V_{N,j}^{global}(r_j) = -\frac{Z_j^s}{2}(3r_c^{-1}-r_c^{-3}r_j^2) \quad \text{for } r_j \leqslant r_c. \tag{46}$$

This is schematically illustrated in Fig. 2. The analytical form [Eqs. (46) and (44)] of the global nucleus potential makes it possible to use an analytic Fourier transform,

$$V_N^{global}(G) = -\sum_j\frac{4\pi Z_j^s e^{-i\mathbf{G}\mathbf{R}_j}}{\sqrt{\Omega}G^2}\left(\frac{3\cos Gr_c}{(Gr_c)^2}-\frac{3\sin Gr_c}{(Gr_c)^3}-\cos Gr_t\right) = -\sum_j\frac{4\pi Z_j^s e^{-i\mathbf{G}\mathbf{R}_j}}{\sqrt{\Omega}}\left(\frac{j_0(Gr_c)+j_2(Gr_c)-\cos Gr_t}{G^2}\right). \tag{47}$$

When the long-ranged screened nucleus potential is truncated the $\mathbf{G}=\mathbf{0}$ term is given by

$$V_N^{global}(\mathbf{0}) = -\sum_j 4\pi Z_j^s (5r_t^2 - r_c^2)/(10\sqrt{\Omega}). \quad (48)$$

Without truncation the $\mathbf{G}=\mathbf{0}$ term diverges. The sum of the divergent terms is finite, however,

$$V_N^{global}(\mathbf{0}) + V_H^{global}(\mathbf{0}) = \sum_j 4\pi Z_j^s r_c^2/(10\sqrt{\Omega}). \quad (49)$$

Therefore, without Coulomb truncation we arbitrarily set $V_H^{global}(\mathbf{0})=0$ and $V_N^{global}(\mathbf{0})=\Sigma_j 4\pi Z_j^s r_c^2/(10\sqrt{\Omega})$. The radial part of the nucleus potential, defined within the atomic spheres only, is given by

$$V_N^{radial}(r_j) = -\frac{Z_j}{r_j} + \frac{Z_j^s}{2}(3r_c^{-1} - r_c^{-3} r_j^2) \quad \text{for } r_j \leq r_c. \quad (50)$$

The total potential V is represented as the sum of a global part V^{global} and a radial part also,

$$V^{global}(\mathbf{G}) = V_N^{global}(G) + V_H^{global}(\mathbf{G}) + V_{xc}^{global}(\mathbf{G}),$$

$$V^{radial}(r_j) = V_N^{radial}(r_j) + V_H^{radial}(r_j) + V_{xc}^{radial}(r_j) \quad \text{for } r_j \leq r_c. \quad (51)$$

It should be noted that V_N^{global} is radially symmetric. $V^{radial}(r_j)$ can be Fourier transformed through

$$V^{radial}(\mathbf{G}) = \sum_j e^{i\mathbf{G}\cdot\mathbf{R}_j} \int_0^{r_c} dr_j 4\pi r_j^2 j_0(Gr_j) V^{radial}(r_j), \quad (52)$$

where $\mathbf{G}$ vectors with high cutoff energy are required. Typical values are 1–2 keV, about an order of magnitude higher than what is required for the plane-wave expansion of the wave functions. The higher value is required for hydrogen as was observed also in FLAPW force calculations.[39] As in the case of the charge density, the total potential can be represented on the global and radial meshes with

$$V_{tot}^{global}(\mathbf{G}) = V^{global}(\mathbf{G}) + \sum_j e^{i\mathbf{G}\cdot\mathbf{R}_j} \int_0^{r_c} dr_j 4\pi r_j^2 j_0(Gr_j) V^{radial}(r_j), \quad (53)$$

$$V_{tot}^{radial}(r_j) = V^{radial}(r_j) + \frac{1}{2\pi G_{max}} \times \int_0^{G_{max}} dG G^2 j_0(Gr_j) \int d\hat{G} e^{-i\mathbf{G}\cdot\mathbf{R}_j} V^{global}(\mathbf{G}). \quad (54)$$

The $\langle \Phi_i | V | \Phi'_j \rangle$ matrix elements between AO's centered on sites i and j are given by

$$\langle \Phi_i | V | \Phi'_j \rangle = \delta_{ij} \left[\sum_{G,G'} \langle \Phi_i | G \rangle \langle G | V^{global} | G' \rangle \langle G' | \Phi'_j \rangle + \langle \Phi_i | V^{radial} | \Phi'_i \rangle \right], \quad (55)$$

but in practice taking the spherical average of the global potential gives accurate results much faster with a one-dimensional integration,

$$\langle \Phi_{inlm} | V | \Phi'_{jn'l'm'} \rangle \approx \langle \Phi_{inlm} | V_{tot}^{radial} | \Phi'_{jn'l'm'} \rangle \approx \delta_{ij}\delta_{ll'}\delta_{mm'} \int_0^{r_c} dr_j r_j^2 R_{nl}(r_j) V_{tot}^{radial}(r_j) R_{n'l}(r_j). \quad (56)$$

It should be noted that because $V_{tot}^{radial}(r_j)$ has angular momentum $l=0$, the matrix elements are diagonal in l and m. Likewise, the $\langle G | V | \Phi_{jnlm} \rangle$ matrix elements can be computed conveniently and accurately using the total radial potential centered on site j with

$$\langle \Phi_{jnlm} | V | \mathbf{G} \rangle = \frac{i^l}{\sqrt{\Omega}} e^{i\mathbf{G}\cdot\mathbf{R}_j} Y_l^m(\hat{G}) \int_0^{r_c} dr_j 4\pi r_j^2 R_l(r_j) V_{tot}^{radial}(r_j) j_l(Gr_j). \quad (57)$$

The $\langle G | V | G' \rangle$ matrix elements can be obtained using Eq. (53).

F. Kinetic energy

The PW-PW matrix elements of the electronic kinetic energy are given simply by $-(G^2/2)\delta_{G,G'}$. The $\langle G | -\nabla^2/2 | \Phi \rangle$ elements are calculated by projecting the AO's onto plane waves using the overlap matrix elements,

$$\langle G | -\frac{\nabla^2}{2} | \Phi \rangle = -\frac{G^2}{2} \langle G | \Phi \rangle. \quad (58)$$

The $\langle \Phi' | -\nabla^2/2 | \Phi \rangle$ elements are computed in real space using

$$\nabla^2(RY) = [R_{rr} + 2r^{-1}R_r - l(l+1)r^{-2}R]Y, \quad (59)$$

where R_r is shorthand for $\partial R_{jnl}/\partial r$. The AO-AO matrix elements of the kinetic energy operator are diagonal in the site j due to the nonoverlapping atomic spheres, and they are diagonal in l and m because of the orthogonality of the spherical harmonics. Simplifying the integrals,

$$\int_0^{r_c} dr r^2 R R_{rr} = \int dS r^2 R R_r - \int_0^{r_c} dr r^2 R_r^2 + 2rRR_r, \quad (60)$$

and using the definition of R [see Eq. (5)] to show that surface integrals such $\int dS r^2 R R_r$ and $\int dS r R^2$ vanish, one obtains

$$-\langle \Phi_{jn'lm} | \nabla^2 | \Phi_{jnlm} \rangle = \int_0^{r_c} dr \frac{\partial r R_{jn'l}}{\partial r} \frac{\partial r R_{jnl}}{\partial r} + l(l+1) R_{jn'l} R_{jnl}, \quad (61)$$

which is easily evaluated using a one-dimensional integration. It should be noted that the $\langle \Phi_{jn'lm} | \nabla^2 | \Phi_{jnlm} \rangle$ elements are not diagonal in the principal quantum number n, in contrast to the AO's themselves. Thus the kinetic energy K is given by

$$K = -\sum_{\lambda} f^{\lambda}\Bigg[\sum_{\mathbf{G}} G^2 c_{\mathbf{G}}^{\lambda *} c_{\mathbf{G}}^{\lambda} + 2\sum_{\mathbf{G}}\sum_{jnlm} G^2 \,\mathrm{Re}[\langle G|\Phi_{jnlm}\rangle c_{\mathbf{G}}^{\lambda *} c_{jnlm}^{\lambda}] + \sum_{jnn'lm} \langle \Phi_{jnlm}|\nabla^2|\Phi_{jn'lm}\rangle c_{jnlm}^{\lambda *} c_{jn'lm}^{\lambda}\Bigg]. \quad (62)$$

G. Total energy and free energy

The total energy is most conveniently computed using the Kohn-Sham eigenvalues,

$$E_{tot} = 2\sum_{\lambda} f^{\lambda}\epsilon^{\lambda} - \frac{1}{2}\int \rho(\mathbf{r}) V_H(\mathbf{r}) d\mathbf{r} - \int \rho(\mathbf{r}) V_{xc}(\mathbf{r}) d\mathbf{r} + E_{xc} + E_{ii}, \quad (63)$$

where $E_{xc} = \int \rho(\mathbf{r}) \epsilon_{xc}(\mathbf{r}) d\mathbf{r}$ is the exchange-correlation energy and E_{ii} represents the Coulomb energy between nuclei, the so-called Madelung energy. In the MB formalism the total energy is evaluated by expanding in global and radial terms,

$$\begin{aligned} E_{tot} = {} & 2\sum_{\lambda} f^{\lambda}\epsilon^{\lambda} - \frac{1}{2}\int \rho^{global}(\mathbf{G}) V_H^{global}(-\mathbf{G}) d\mathbf{G} \\ & - \int \rho^{radial}(\mathbf{G}) V_H^{global}(-\mathbf{G}) d\mathbf{G} \\ & - 2\pi \int r^2 \rho^{radial}(r) V_H^{radial}(r) dr + \int \rho^{global}(\mathbf{r}) \gamma_{xc}^{global}(\mathbf{r}) d\mathbf{r} \\ & + \int \rho^{global}(\mathbf{G}) \gamma_{xc}^{radial}(-\mathbf{G}) d\mathbf{G} \\ & + \int \rho^{radial}(\mathbf{G}) \gamma_{xc}^{global}(-\mathbf{G}) d\mathbf{G} \\ & + 4\pi \int r^2 \rho^{radial}(r) \gamma_{xc}^{radial}(r) dr + E_{ii} + E_{cc}, \end{aligned} \quad (64)$$

where $\gamma_{xc} = \epsilon_{xc} - V_{xc}$. The long-ranged part of the radial Hartree potential gives rise to a core-core Coulomb term E_{cc}, which is of the same form as the ion-ion term if it is assumed that the radial charge density within an atomic sphere is well represented by a point charge,

$$E_{ii} = \frac{1}{2}\sum_{k\neq j} \frac{Z_j Z_k}{|\mathbf{R}_j - \mathbf{R}_k|}, \quad E_{cc} = -\frac{1}{2}\sum_{k\neq j} \frac{Q_j Q_k}{|\mathbf{R}_j - \mathbf{R}_k|}, \quad (65)$$

where Q_j is the radial electronic charge within the atomic sphere j given by Eq. (42) and j and k refer to atoms inside and outside the unit cell. Usually these sums are evaluated with the Ewald method, but when the Coulomb potential is truncated the sums are limited to ions k and j within the unit cell only so that a simple summation suffices.

If there is a small or vanishing gap, it frequently happens that states near the Fermi level switch between occupied and unoccupied from one self-consistency iteration to the next. In such a case it is advantageous to use broadening by considering nonzero electron temperatures. In metals and at finite temperatures partial occupancies occur so that the contribution of the electronic entropy S^e must be taken into account,

$$S^e = -2k_B \sum_{\lambda} [f^{\lambda} \ln(f^{\lambda}) + (1 - f^{\lambda}) \ln(1 - f^{\lambda})]. \quad (66)$$

The total energy is the proper thermodynamic potential only when $T^e = 0$; at nonzero temperature, the free energy should be used,[40,41]

$$\Theta = E_{tot} - T^e S^e. \quad (67)$$

Expression (64) is not expedient for the derivation of the forces. Then, it is better to use

$$E_{tot} = K + W + E_{ii}, \quad (68)$$

where K and W represent the kinetic and potential energy, respectively, of the electrons. The potential energy W is given by

$$W = \int d\mathbf{r} \rho(\mathbf{r}) \left[V_N(\mathbf{r}) + \frac{1}{2} V_H(\mathbf{r}) + \epsilon_{xc} \right]. \quad (69)$$

As in Eq. (64) this expression can be decomposed in contributions on the radial and global meshes.

H. Force calculation

The force calculation follows the earlier work for the pseudopotential MB method by Ho *et al.*[26] but has been adjusted for the present all-electron formalism. The current derivation is similar also to the force calculation in the LAPW method by Yu *et al.*[42] except that the muffin-tin surface contribution [Eq. (20b) in Ref. 42] can be made to vanish trivially in the MB method by imposing boundary conditions on the radial part of the atomic orbitals [see Eq. (5)]. The force F on atom j can be expressed in terms of partial derivatives as follows:

$$\mathbf{F}_j = -\frac{d\Theta}{d\mathbf{R}_j} = -\left(\frac{\partial \Theta}{\partial \mathbf{R}_j}\right)_{c,f} - \left(\frac{\partial \Theta}{\partial c}\right)_{R,f} \left(\frac{\partial c}{\partial \mathbf{R}_j}\right)_f - \left(\frac{\partial \Theta}{\partial f}\right)_{R,c} \left(\frac{\partial f}{\partial \mathbf{R}_j}\right)_c, \quad (70)$$

where the notation for partial derivatives as is customary in thermodynamics is employed.[43] The first term on the right-hand side (RHS) corresponds to the usual Hellmann-Feynman force, and the second term gives rise to the so-called incomplete basis set force,[44–47] while the third term vanishes because the electronic free energy is minimal with respect to the occupation numbers; see also Ref. 41.

As was shown by Weinert and Davenport[41] there is no contribution from the electronic entropy term $-TS$ to the force so that the Hellmann-Feynman force can be divided into three parts, a contribution (1) from the kinetic energy, (2) from the product of total potential and electronic charge density, and (3) from the ionion energy. The kinetic energy contribution is calculated easily using Eqs. (58) and (61),

$$\left(\frac{\partial K}{\partial \mathbf{R}_j}\right)_{c,f} = -\frac{1}{2}\left(\frac{\partial}{\partial \mathbf{R}_j}\right)\sum_{c,f}\sum_{\lambda} f^{\lambda}\Bigg[\sum_{pnlm,n'} c^{\lambda*}_{pnlm}c^{\lambda}_{pn'lm}\langle\Phi_{pnlm}|\nabla^2|\Phi_{pn'lm}\rangle + \sum_{pnlm,\mathbf{G}} c^{\lambda*}_{pnlm}c^{\lambda}_{\mathbf{G}}G^2\langle\Phi_{pnlm}|\mathbf{G}\rangle + c^{\lambda*}_{\mathbf{G}}c^{\lambda}_{pnlm}G^2\langle\mathbf{G}|\Phi_{pnlm}\rangle + \sum_{\mathbf{G}} c^{\lambda*}_{\mathbf{G}}c^{\lambda}_{\mathbf{G}}G^2\Bigg]. \quad (71)$$

Clearly, the only $\mathbf{R}_j$ dependence derives from the overlap elements $\langle\mathbf{G}|\Phi_{pnlm}\rangle$ and its complex conjugate. Equation (12) shows that

$$\left(\frac{\partial\langle\mathbf{G}|\Phi_{pnlm}\rangle}{\partial \mathbf{R}_j}\right)_{c,f} = i\mathbf{G}\langle\mathbf{G}|\Phi_{jnlm}\rangle, \quad (72)$$

so that

$$\left(\frac{\partial K}{\partial \mathbf{R}_j}\right)_{c,f} = \sum_{\lambda} f^{\lambda}\sum_{nlm,\mathbf{G}} \mathbf{G}G^2\,\mathrm{Im}[c^{\lambda*}_{\mathbf{G}}c^{\lambda}_{jnlm}\langle\mathbf{G}|\Phi_{jnlm}\rangle], \quad (73)$$

where "Im" indicates the imaginary part.

The force contribution of the potential energy W arises from two sources: (i) the phase factors in the integrals over products of radial and global properties and (ii) the explicit $\mathbf{R}_j$ dependence in the PW-AO contribution to the radial charge density as evidenced in Eq. (25). First, the contribution from the phase factors is examined,

$$\left(\frac{\partial W}{\partial \mathbf{R}_j}\right)_{c,f} = \left(\frac{\partial}{\partial \mathbf{R}_j}\right)_{c,f}\int d\mathbf{G}V_N(-\mathbf{G})\rho(\mathbf{G}) + \frac{1}{2}V_H(-\mathbf{G})\rho(\mathbf{G}) + \epsilon_{xc}(-\mathbf{G})\rho(\mathbf{G}). \quad (74)$$

The nuclear part contributes only when the global charge density is involved,

$$\left(\frac{\partial}{\partial \mathbf{R}_j}\right)_{c,f}\int d\mathbf{G}V_N(-\mathbf{G})\rho(\mathbf{G}) = -4\pi\left(\frac{\partial}{\partial \mathbf{R}_j}\right)\sum_{c,f}\sum_{k}\int d\mathbf{G}\frac{Z_k}{G^2}e^{-i\mathbf{G}\cdot\mathbf{R}_k}\rho^{global}(\mathbf{G}) = -4\pi\int d\mathbf{G} - i\mathbf{G}\frac{Z_j}{G^2}e^{-i\mathbf{G}\cdot\mathbf{R}_j}\rho^{global}(\mathbf{G}) = -\int d\mathbf{G}GZ_j\,\mathrm{Im}[e^{i\mathbf{G}\cdot\mathbf{R}_j}V^{global}_H(-\mathbf{G})]. \quad (75)$$

The Hartree part can be analyzed along similar lines,

$$\left(\frac{\partial}{\partial \mathbf{R}_j}\right)_{c,f}\int d\mathbf{G}\frac{1}{2}V_H(-\mathbf{G})\rho(\mathbf{G}) = 2\pi\left(\frac{\partial}{\partial \mathbf{R}_j}\right)\sum_{c,f}\sum_{k}\int d\mathbf{G}\left[\frac{\rho^{radial}_k(-\mathbf{G})}{G^2}e^{-i\mathbf{G}\cdot\mathbf{R}_k}\rho^{global}(\mathbf{G}) + \frac{\rho^{global}(-\mathbf{G})}{G^2}e^{i\mathbf{G}\cdot\mathbf{R}_k}\rho^{radial}_k(\mathbf{G})\right] = \int d\mathbf{G}G\rho^{radial}_j(\mathbf{G})\mathrm{Im}[V^{global}_H(-\mathbf{G})e^{i\mathbf{G}\cdot\mathbf{R}_j}]. \quad (76)$$

The exchange correlation part is most apparent by first differentiating with respect to the charge density,

$$\left(\frac{\partial}{\partial \mathbf{R}_j}\right)_{c,f}\int d\mathbf{r}\epsilon_{xc}(\mathbf{r})\rho(\mathbf{r}) = \int d\mathbf{r}\frac{d\epsilon_{xc}(\mathbf{r})\rho(\mathbf{r})}{d\rho(\mathbf{r})}\left(\frac{\partial\rho(\mathbf{r})}{\partial \mathbf{R}_j}\right)_{c,f} = \int d\mathbf{r}V_{xc}(\mathbf{r})\left(\frac{\partial\rho(\mathbf{r})}{\partial \mathbf{R}_j}\right)_{c,f} = \int d\mathbf{G}V_{xc}(-\mathbf{G})\left(\frac{\partial\rho(\mathbf{G})}{\partial \mathbf{R}_j}\right)_{c,f} = \int d\mathbf{G}G\rho^{radial}_j(\mathbf{G})\mathrm{Im}[V^{global}_{xc}(-\mathbf{G})e^{i\mathbf{G}\cdot\mathbf{R}_j}]. \quad (77)$$

The contribution from the explicit $\mathbf{R}_j$ dependence in the PW-AO part of the radial charge density is determined as follows:

$$\int d\mathbf{r}\frac{d\{[V_N(\mathbf{r}) + \frac{1}{2}V_H(\mathbf{r}) + \epsilon_{xc}(\mathbf{r})]\rho(\mathbf{r})\}}{d\rho}\left(\frac{\partial\rho(\mathbf{r})}{\partial \mathbf{R}_j}\right)_{c,f} = \int d\mathbf{r}[V_N(\mathbf{r}) + V_H(\mathbf{r}) + V_{xc}(\mathbf{r})]\left(\frac{\partial\rho(\mathbf{r})}{\partial \mathbf{R}_j}\right)_{c,f} = \int d\mathbf{r}V_{total}(\mathbf{r})\left(\frac{\partial\rho(\mathbf{r})}{\partial \mathbf{R}_j}\right)_{c,f} = \int d\mathbf{r}V_{total}(\mathbf{r})\sum_{k}\left(\frac{\partial\rho^{PW\,AO}_k(\mathbf{r})}{\partial \mathbf{R}_j}\right)_{c,f} = \frac{4}{\sqrt{\Omega}}\sum_{\mathbf{G}}\mathbf{G}\sum_{nlm}\mathrm{Im}\left[i^l Y^m_l(\hat{G})e^{i\mathbf{G}\cdot\mathbf{R}_j}\sum_{\lambda} f^{\lambda}c^{\lambda}_{\mathbf{G}}c^{\lambda*}_{jnlm}\right] \times \int dr_j j_l(Gr_j)V^{radial}_{total}(r_j)R_{jnl}(r_j). \quad (78)$$

The force from the electronic potential energy can hence be written as

$$\left(\frac{\partial W}{\partial \mathbf{R}_j}\right)_{c,f} = \int d\mathbf{G}G(\rho^{radial}_j(\mathbf{G}) - Z_j)\mathrm{Im}[V^{global}_H(-\mathbf{G})e^{i\mathbf{G}\cdot\mathbf{R}_j}] + \int d\mathbf{G}G\rho^{radial}_j(\mathbf{G})\mathrm{Im}[V^{global}_{xc}(-\mathbf{G})e^{i\mathbf{G}\cdot\mathbf{R}_j}] + \frac{4}{\sqrt{\Omega}}\sum_{\mathbf{G}}\mathbf{G}\sum_{nlm}\mathrm{Im}\left[i^l Y^m_l(\hat{G})e^{i\mathbf{G}\cdot\mathbf{R}_j}\sum_{\lambda} f^{\lambda}c^{\lambda}_{\mathbf{G}}c^{\lambda*}_{jnlm}\right] \times \int dr_j j_l(Gr_j)V^{radial}_{total}(r_j)R_{jnl}(r_j). \quad (79)$$

The Madelung contribution to the Hellmann-Feynman force is obtained by differentiating the Ewald summation,

$$\left(\frac{\partial}{\partial \mathbf{R}_j}\right)_{c,f} \frac{1}{2}\sum_{p,q} Z_p^s Z_q^s \sum_{\mathbf{T}} \frac{(1-\delta_{\mathbf{T},\mathbf{0}}\delta_{p,q})}{|\mathbf{R}_p-\mathbf{R}_q+\mathbf{T}|}$$
$$= -\sum_q Z_j^s Z_q^s \Bigg[\sum_{\mathbf{T}} (1-\delta_{\mathbf{T},\mathbf{0}}\delta_{j,q}) \frac{(\mathbf{R}_j-\mathbf{R}_q+\mathbf{T})}{|\mathbf{R}_j-\mathbf{R}_q+\mathbf{T}|^2}$$
$$\times \left(\frac{2\eta}{\sqrt{\pi}} \exp(-\eta^2 |\mathbf{R}_j-\mathbf{R}_q+\mathbf{T}|^2) + \frac{\mathrm{erfc}(\eta|\mathbf{R}_j-\mathbf{R}_q+\mathbf{T}|)}{|\mathbf{R}_j-\mathbf{R}_q+\mathbf{T}|} \right)$$
$$+ \frac{4\pi}{\Omega} \sum_{\mathbf{G}\neq 0} \frac{\mathbf{G}}{|\mathbf{G}|^2} \exp(-|\mathbf{G}|^2\eta^{-2}/4) \sin[(\mathbf{R}_j-\mathbf{R}_q)\cdot\mathbf{G}] \Bigg], \tag{80}$$

or, in case the Coulomb potential is truncated, by differentiating the direct sum,

$$\left(\frac{\partial}{\partial \mathbf{R}_j}\right)_{c,f} \frac{1}{2}\sum_{p,q} \frac{Z_p^s Z_q^s}{|\mathbf{R}_p-\mathbf{R}_q|} = -\sum_q \frac{Z_j^s Z_q^s}{|\mathbf{R}_j-\mathbf{R}_q|^2} \frac{\mathbf{R}_j-\mathbf{R}_q}{|\mathbf{R}_j-\mathbf{R}_q|}, \tag{81}$$

where the screened nuclear charge is used because the long-ranged radial Hartree potential is combined with the nuclear potential as set forth in Eq. (42).

Aside from the usual Hellmann-Feynman force, the incomplete basis set force must be considered,

$$\sum_{\lambda,\nu} \left(\frac{\partial \Theta}{\partial c_\nu^\lambda}\right)_{R,f} \frac{\partial c_\nu^\lambda}{\partial \mathbf{R}_j} + \text{c.c.} = \sum_\lambda f^\lambda \sum_{\mu,\nu} c_\mu^{\lambda *} H_{\mu\nu} \frac{\partial c_\nu^\lambda}{\partial \mathbf{R}_j} + \text{c.c.}$$
$$= \sum_\lambda f^\lambda \epsilon^\lambda \sum_{\mu,\nu} c_\mu^{\lambda *} S_{\mu\nu} \frac{\partial c_\nu^\lambda}{\partial \mathbf{R}_j} + \text{c.c.}$$
$$= -\sum_\lambda f^\lambda \epsilon^\lambda \sum_{\mu,\nu} c_\mu^{\lambda *} \frac{\partial S_{\mu\nu}}{\partial \mathbf{R}_j} c_\nu^\lambda, \tag{82}$$

where the orthonormalization condition $\Sigma_{\mu,\nu} c_\mu^{\lambda *} S_{\mu\nu} c_\nu^\lambda = 1$ has been used. The overlap matrix element is a function of $\mathbf{R}_j$ only if it is between a plane wave and an atomic orbital on site j as is apparent from Eq. (72) which gives

$$\sum_{\lambda,\nu} \left(\frac{\partial \Theta}{\partial c_\nu^\lambda}\right)_{R,f} \frac{\partial c_\nu^\lambda}{\partial \mathbf{R}_j} + \text{c.c.}$$
$$= -\sum_\lambda f^\lambda \epsilon^\lambda \sum_{\mathbf{G},nlm} c_{\mathbf{G}}^{\lambda *} i\mathbf{G} S_{\mathbf{G}jnlm} c_{jnlm}^\lambda + \text{c.c.}$$
$$= -2\sum_\lambda f^\lambda \epsilon^\lambda \sum_{\mathbf{G},nlm} \mathbf{G}\, \mathrm{Im}[c_{\mathbf{G}}^{\lambda *} S_{\mathbf{G}jnlm} c_{jnlm}^\lambda]. \tag{83}$$

Comparison with Eq. (73) shows that the kinetic energy contribution to the Hellmann-Feynman force has a very similar form as the incomplete basis set force. The atomic forces are now computed by evaluating Eqs. (73), (83), (79), and (80) or (81).

I. Hyperfine tensor

One of the advantages of all-electron methods is that properties associated with core levels are readily computed. Here, the computation of the hyperfine tensor will be written out in some detail. The hyperfine tensor **A** can be divided into the Fermi contact interaction a and the dipole interaction **b**,

$$A_{\alpha\beta} = a\delta_{\alpha\beta} + b_{\alpha\beta}, \tag{84}$$

where the subscripts α, β refer to Cartesian coordinates x, y, and z. The Fermi contact interaction is proportional to the spin density $\rho_s(\mathbf{R}_j) = \rho_\uparrow(\mathbf{R}_j) - \rho_\downarrow(\mathbf{R}_j)$ at the nucleus $\mathbf{R}_j$,

$$a_j = \frac{2}{3}\mu_0 g_e \mu_e g_j \mu_j \rho_s(\mathbf{R}_j), \tag{85}$$

where μ_0 is the permeability of vacuum ($4\pi\times10^{-7}$ $\mathrm{T^2\,m^3\,J^{-1}}$), g_e is the electron g factor, μ_e is the Bohr magneton, and g_j and μ_j are the gyromagnetic ratio and the magnetic moment of the nucleus j. Throughout this work, g_j and μ_j values are taken from Ref. 48. The spin density at the nucleus is trivially computed from the charge densities as given by Eqs. (21), (25), and (26). The dipole part is a function of the spin density also,

$$b_{j,\alpha\beta} = \frac{1}{4\pi}\mu_0 g_e \mu_e g_j \mu_j \int d\mathbf{r}_j \frac{\rho_{s,j}(\mathbf{r}_j)}{r_j^3} T_{\alpha\beta}$$
$$\text{with } T_{\alpha\beta} = \frac{3x_\alpha x_\beta - r_j^2\delta_{\alpha\beta}}{r_j^2}. \tag{86}$$

The tensor **T** can be easily expressed in terms of real spherical harmonics $\tilde{Y}$,

$$\mathbf{T} = \sqrt{\frac{12\pi}{5}} \begin{pmatrix} \tilde{Y}_2^2 - \sqrt{1/3}\tilde{Y}_2^0 & -\tilde{Y}_2^{-2} & -\tilde{Y}_2^1 \\ -\tilde{Y}_2^{-2} & -\tilde{Y}_2^2 - \sqrt{1/3}\tilde{Y}_2^0 & -\tilde{Y}_2^{-1} \\ -\tilde{Y}_2^1 & -\tilde{Y}_2^{-1} & \sqrt{4/3}\tilde{Y}_2^0 \end{pmatrix}, \tag{87}$$

so that the dipole interaction can be computed conveniently with

$$b_{j,\alpha\beta} = \frac{1}{4\pi}\mu_0 g_e \mu_e g_j \mu_j \int dr_j \sum_{M=-2}^{2} \frac{\rho_{s,jLM}(r_j)}{r_j} \int d\hat{r}_j Y_L^{M*}(\hat{r}_j) T_{\alpha\beta}$$
$$\text{with } L = 2. \tag{88}$$

Note that the integral over $\hat{r}_j$ is trivial because spherical harmonics are orthonormal. Hence, a one-dimensional integral remains. The LM-decomposed AO-AO and PW-AO charge densities have been derived already [see Eqs. (23) and (24)], and the PWPW part is derived as.

$$\sum_{lm} \rho_{jlm}^{PW\ PW}(r_j) Y_l^m(\hat{r}_j) = \int d\mathbf{G} e^{-i\mathbf{G}\cdot\mathbf{R}_j} e^{-i\mathbf{G}\cdot\mathbf{r}_j} \rho^{PW\ PW}(\mathbf{G}), \tag{89}$$

where $\mathbf{r}_j$ is understood to go beyond the sphere j because a significant part of the spin density may be outside (between) the atomic spheres. After multiplying with $Y_l^{m*}(\hat{r}_j)$ and integrating over $\hat{r}_j$, while substituting Eq. (11), this becomes

$$\rho_{jlm}^{PW\ PW}(r_j) = 4\pi \int d\mathbf{G} e^{-i\mathbf{G}\cdot\mathbf{R}_j} i^{-l} j_l(Gr_j) Y_l^m(\hat{G}) \rho^{PW\ PW}(\mathbf{G}). \tag{90}$$

Alternately, the PW-PW contribution to b can be computed directly by evaluating Eq. (86) directly in real space.

Since the hyperfine tensor $\mathbf{A}$ is symmetric, one can diagonalize it in terms of two perpendicular $A_\perp$ and one parallel $A_\parallel$ components. Then, the anisotropic HFP A_{aniso} is expressed as $A_{aniso}=A_\parallel - A_\perp$.

Although relativistic corrections have not been considered in this work, we explicitly mention that there is an elegant formalism for including scalar relativistic effects.[49] Blügel *et al.*[49] have shown that to first order scalar relativistic corrections to the Fermi-contact hyperfine field can be obtained by replacing the spin density at the nucleus position $\rho_s(\mathbf{R}_j)$ in Eq. (85) with an average $\rho_s(\mathbf{R}_j)$ computed over a small sphere centered on that nucleus with a radius of the order of the Thomson radius, $r_T=Z_j e^2/mc^2$, where m and c are the electron mass and speed of light in vacuum, respectively, according to

$$\rho_s(\mathbf{R}_j) = \int d\mathbf{r} \rho_s(\mathbf{R}_j + \mathbf{r}) \delta(\mathbf{r}), \tag{91}$$

where $\delta(\mathbf{r})$ is a smeared-out delta function, as

$$\delta(\mathbf{r}) = \frac{1}{4\pi r^2} \frac{r_T/2}{(r + r_T/2)^2}. \tag{92}$$

The implementation of the second and higher order relativistic corrections such as the spin-orbit interaction requires much more sophisticated methods—e.g., transformed Hamiltonian methods. Such methods have their own difficulties accurately representing the spin density in the vicinity of nucleus.[50]

J. Spin-polarization mechanism of core levels

It is well known that in some cases the effective magnetic field at the nucleus is opposite to the spin polarization.[51] This somewhat counterintuitive finding has been explained in detail for ferromagnetic iron in terms of spin-dependent deformation of core-level s orbitals as a result of interaction with spin-polarized valence states.[52]

Here we analyze the spin-polarization mechanism of core s levels within the DFT formalism. In order to give a qualitative picture of the driving force of this mechanism and clarify how each core s level contributes to the spin density at the nucleus, we use first-order perturbation theory to construct the spin-polarized wave function $\tilde{\Psi}_\sigma^\lambda$ from a linear combination of non-spin-polarized eigenstates Ψ^λ. Throughout this paper σ indicates the spin sign: it takes the value +1 (−1) for majority spin up (minority spin down), and it is labeled with an upward (downward) arrow subscript.

As a starting point, we consider that the spin polarization induces a perturbing potential ΔV_σ, so that the first-order perturbation of energy, $\Delta\tilde{\varepsilon}_\sigma^\lambda$, and wave function $\tilde{\Psi}_\sigma^\lambda$ are given as

$$\Delta\tilde{\varepsilon}_\sigma^\lambda = \langle \Psi^\lambda | \Delta V_\sigma | \Psi^\lambda \rangle, \tag{93}$$

$$|\tilde{\Psi}_\sigma^\lambda\rangle = |\Psi^\lambda\rangle + \sigma \sum_{\lambda\neq\kappa} C^{\lambda\kappa} |\Psi^\kappa\rangle, \tag{94}$$

where we have used the fact that the perturbing potential ΔV_σ differs just in sign for the spin-up and spin-down channels [see Eq. (103)] so that

$$C^{\lambda\kappa} = \sigma \frac{\langle \Psi^\kappa | \Delta V_\sigma | \Psi^\lambda \rangle}{\varepsilon^\lambda - \varepsilon^\kappa} \tag{95}$$

does not depend on σ. Equations (94) and (95) suggest that only levels κ need to be taken into account which are energetically close to the given level λ and for which $\langle \Psi^\kappa | \Delta V_\sigma | \Psi^\lambda \rangle$ is considerable. Additionally, Eq. (95) implies that $C^{\lambda\kappa}$ should have real values for given s orbitals λ and κ and that $C^{\lambda\kappa}=-C^{\kappa\lambda}$.

The spin density at the nucleus derived from a certain s-type core level can be related to the perturbed wave functions and the C coefficients with

$$\rho_s^\lambda(\mathbf{r}) = \rho_\uparrow^\lambda(\mathbf{r}) - \rho_\downarrow^\lambda(\mathbf{r}) = 4\Psi^\lambda(\mathbf{r}) \sum_{\kappa\neq\lambda} C^{\lambda\kappa} \Psi^\kappa(\mathbf{r}). \tag{96}$$

As we shall consider only s-type core levels, which have positive radial wave functions at the nucleus, it follows that if the C coefficients are positive, the spin density at the nucleus is of the same sign as the overall spin polarization and vice versa. To determine whether a given level λ has a positive or negative contribution to the isotropic HFP comes down to determining the sign and magnitude of the $C_{\lambda\kappa}$ coefficients. When Eq. (96) is summed over all levels λ and considering that $C^{\lambda\kappa}$ changes sign under reversal of the superscripts, it is apparent that Eq. (96) gives a vanishing net spin polarization at the nucleus. In other words, while our simple first-order perturbation gives insight into the contributions from individual levels to the spin density at the nucleus, it is too crude to formulate the effect of the total core polarization.

Equation (95) shows that $C^{\lambda\kappa}$ depends on ΔV_σ. Here, we use DFT to define ΔV_σ in terms of the total charge density and the spin density. Our argument is based on the fact that the spin polarization of the Kohn-Sham levels originates from the spin-dependent effective potential $V_{eff,\sigma}(\mathbf{r})$. The effective potential $V_{eff,\sigma}(\mathbf{r})$, in the absence of external fields, is defined analogously to Eq. (14) as

$$V_{eff,\sigma}(\mathbf{r}) = V_N(\mathbf{r}) + V_H(\mathbf{r}) + V_{xc,\sigma}(\mathbf{r}). \tag{97}$$

Equation (97) reveals that the exchange-correlation potential $V_{xc,\sigma}(\mathbf{r})$ is the only term which is spin dependent. This term can be separated into exchange and correlation contributions, $V_{xc,\sigma}(\mathbf{r})=V_{x,\sigma}(\mathbf{r})+V_{c,\sigma}(\mathbf{r})$. As there is no transparent way to define a spin-decomposed form of the correlation potential $V_{c,\sigma}(\mathbf{r})$, we retain only the exchange potential $V_{x,\sigma}(\mathbf{r})$. In any case the contribution of $V_{c,\sigma}(\mathbf{r})$ to the effective potential difference ΔV_{eff} is expected to be negligible.[53]

Following the LSDA method,[54] the exchange potential is expressed as[55]

$$V_{x,\sigma}(\mathbf{r}) = \frac{\partial E_x[\rho_\uparrow, \rho_\downarrow]}{\partial \rho_\sigma(\mathbf{r})}, \tag{98}$$

where

$$E_x[\rho_\uparrow, \rho_\downarrow] = -\frac{9}{4}\alpha\left(\frac{3}{4\pi}\right)^{1/3} \int [(\rho_\uparrow)^{4/3} + (\rho_\downarrow)^{4/3}] d\mathbf{r}, \tag{99}$$

where α has the units (energy length)/charge$^{4/3}$, for the homogeneous free electron gas $\alpha = 2/3$ in atomic units.[56] As is common in the literature, below we will assume atomic units and fold $\alpha = 2/3$ into the numerical factor, which gives

$$V_{x\sigma} \simeq -2^{1/3}\left(\frac{3}{\pi}\right)\rho_\sigma^{1/3}. \tag{100}$$

Defining the spin-polarization parameter ζ as

$$\zeta = \frac{\rho_\uparrow - \rho_\downarrow}{\rho_\uparrow + \rho_\downarrow} = \frac{\rho_\uparrow - \rho_\downarrow}{\rho}, \tag{101}$$

Eq. (100) becomes

$$V_{x\sigma} \simeq -\frac{3}{\pi}(1 + \sigma\zeta)^{1/3}\rho^{1/3} \tag{102}$$

and the change due to the spin polarization is given by the first-order term of a Taylor series in ζ:

$$\Delta V_{x\sigma} \simeq -\frac{\sigma}{\pi}\rho^{1/3}\zeta + O(\zeta^2). \tag{103}$$

It is to be noted that the perturbing potential differs only in sign for the two spin channels, as mentioned above Eq. (95). As Eq. (103) is the first-order term, it is valid for small values of ζ only. Near the nucleus this should be a good approximation, but far from the nucleus, where ζ takes large values, Eq. (103) should be less accurate. The effective potential difference

$$\Delta V_{eff} = \Delta V_{x\uparrow} - \Delta V_{x\downarrow} \simeq -\frac{2}{\pi}\rho^{1/3}\zeta \tag{104}$$

is given in terms of the spin-polarization parameter ζ and the total density ρ. Recalling our convention that the majority spin is defined as spin up and indicating the singly occupied valence levels as "SOVO," Eq. (104) can be written as

$$\Delta V_{eff} \simeq -\frac{2}{\pi}\frac{(\rho_\uparrow - \rho_\downarrow)}{\rho^{2/3}} \simeq -\frac{2}{\pi}\frac{\rho^{SOVO}}{\rho^{2/3}}. \tag{105}$$

Equation (105) states that $\Delta V_{eff}(\mathbf{r})$ depends sensitively on the type of SOVO. Figure 3 illustrates the radial $l=0$ component of $\Delta V_{eff}(\mathbf{r})$ obtained directly from a Kohn-Sham DFT calculation and as obtained from Eq. (105) for Ca^+ with a $4s$-type SOVO and for Mn with a $3d$-type SOVO. It shows that the approximate expression is of adequate accuracy to serve for purposes of qualitative analysis, and it shows that $\Delta V_{eff}(\mathbf{r})$ of Mn is far more localized than $\Delta V_{eff}(\mathbf{r})$ of Ca^+. Clearly, strong spin polarization of core levels is expected for systems such as Mn with a $3d$-type SOVO while for cases such as Ca^+ the spin polarization of core levels is weak. Quite generally, the SOVO for which the difference of the principal and angular momentum quantum numbers is unity should be close to the nucleus and causing the strongest core spin polarization.

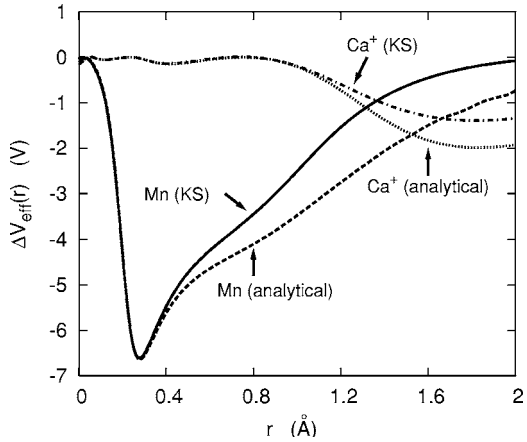

FIG. 3. Comparison of $\Delta V_{eff}(r)$ obtained directly with $V_{eff\uparrow} - V_{eff\downarrow}$ from a Kohn-Sham DFT calculation (marked with "KS") and as computed with Eq. (105) (marked with "analytical") for Ca^+ and Mn.

As the perturbing potential for spin majority ($\uparrow$) and spin minority ($\downarrow$) are just different in sign, one can analyze the effect of ΔV_{eff} by considering the effect of the perturbing term $\Delta V_\uparrow$ on the spin-majority states only. Examination of the value of $C^{\lambda\kappa}$ shows that the denominator in Eq. (95) is negative (positive) when level λ lies lower (higher) than level κ, while for the numerator a more detailed analysis is called for. The $l=0$ radial integrand in the numerator of Eq. (95) can be written as

$$\Delta V_\uparrow^{\kappa\lambda}(r) = \Psi^\kappa(r)\Delta V_\uparrow(r)\Psi^\lambda(r)r^2 = \Delta V_\uparrow(r)F^{\lambda\kappa}(r), \tag{106}$$

where the radial overlap function is given as

$$F^{\lambda\kappa}(r) = \Psi^\lambda(r)\Psi_\kappa(r)r^2. \tag{107}$$

We use the word "overlap" somewhat freely to indicate that radial functions take large values at the same distance from the nucleus. It is important to emphasize that the angular momentum character does not enter in this discussion because a SOVO with $l \neq 0$ contributes to a perturbing potential with $l=0$, so that all radial functions involved pertain to $l=0$. Orthogonality of eigenstates, and the fact that we will look at $l=0$ core levels only, makes the radial integration over the radial overlap function vanish for $\lambda \neq \kappa$. As $\Delta V_\uparrow$ is negative, the radial integrand of Eq. (106) is negative when $\Delta V_\uparrow(r)$ has a large magnitude for r where the radial overlap function is positive. In contrast, the integrand is positive when $\Delta V_\uparrow(r)$ is more localized at r values where the radial overlap function is negative. The radial overlap function can be understood on the basis of atomic calculations, while the perturbing potential is related to the SOVO through Eq. (105) so that now we can qualitatively analyze the sign contribution of each $\Psi^\kappa(\mathbf{r})$ to the $\tilde{\Psi}^{\kappa\uparrow}(\mathbf{r})$ in Eq. (94). Below, we apply this analysis of systems with $3d$-type and $4s$-type SOVO.

The derivation of the effective perturbing potential also makes it straightforward to analyze the difference between eigenvalues of spin-majority and spin-minority core levels by inserting Eqs. (105) and (103) into Eq. (93):

$$\Delta\tilde{\varepsilon}_{\sigma}^{\lambda} \simeq -\langle\Psi^{\lambda}|\frac{\sigma}{\pi}\frac{\rho^{SOVO}}{\rho^{2/3}}|\Psi^{\lambda}\rangle \simeq -\sigma\int 4r^2 dr\rho^{\lambda}(r)\frac{\rho^{SOVO}(r)}{\rho^{2/3}(r)}. \tag{108}$$

It is apparent that spin-majority core levels move towards lower energies while spin-minority core levels become less strongly bound.

III. COMPUTATIONAL METHOD

In this work the DFT calculations have been carried out within the LSDA.[38] In the MB formalism there are a number of parameters which must be selected with care. Some parameters, such as the cutoff energy of the PW expansion of the potential, are important for accurately computing the forces and thus affect the final geometry, but turn out to be rather unimportant for the HFP's when the correct geometry is used. Accurate forces were obtained with a potential cutoff energy of about 1000 eV for all elements considered with a single exception. For hydrogen a higher value of 1500–2000 eV is required, as was observed within the full-potential linearized augmented plane-wave method also.[39] Among the HFP's, it turns out that the Fermi contact interaction is far more sensitive to the choice of parameters than the anisotropic HFP's. Therefore, below we shall focus on the effect of computational parameters on the Fermi contact interaction. The AO's used for expanding the one-electron Kohn-Sham wave functions are obtained from non-spin-polarized atomic calculations. Generally, we select the ground-state electronic occupation numbers for the atomic calculation. However, for ions we have found that more rapidly converging results are obtained if the AO's are derived from an atomic calculation with electronic occupation numbers that mimic the ion. Thus, for 1+ ions belonging to group II of the periodic table we selected a non-ground-state electronic configuration with one outer s electron and one outer p ($^{25}Mg^{+}$) or d ($^{43}Ca^{+}$) electron. The outer p or d atomic orbital can be retained in the MB expansion for the wave functions but this has little effect on the computed HFP's. For the single-atom and single-ion calculations we selected a rather large atomic sphere size with a radius of ~3 Å. Using this rather large size allowed optimal use of the AO's for the more extended outer s-like states which benefits the accurate computation of the Fermi contact interaction. Other important parameters are supercell size and PW cutoff energy for the expansion of the wave functions.

Figure 4 indicates the convergence of the calculated Fermi contact interaction of the ^{7}Li atom with respect to supercell size. The cutoff energy for the PW expansion of the wave functions is 200 eV. A supercell size of 12 Å gives converged results that are in excellent agreement with experiment.[57] The supercell size plays an important role for atomic ^{7}Li because of the spatial range of the 2s wave function. For small supercells, the tails of the 2s wave functions overlap with neighboring cells, which in turn affects the 1s wave function. For other atomic calculations the 12 Å size has appeared sufficiently large also to assure convergence of the Fermi contact interaction. Spatially extended clusters require larger supercell sizes, and a 12-Å separation distance is a guideline.

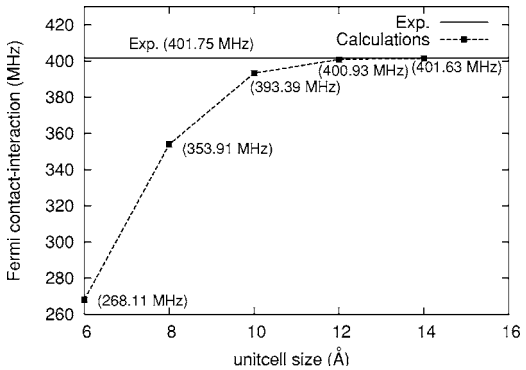

FIG. 4. Computed Fermi contact interaction for atomic ^{7}Li as a function of supercell size. The experimental value is from Ref. 57.

Figure 5 shows the dependence of the Fermi contact interaction of ^{7}Li sample on the cutoff energy of the PW expansion of the wave functions. Clearly, the PW cutoff energy plays a minor role when compared to the supercell size. It appears that at a cutoff energy of 200 eV the wave functions are described with sufficient accuracy provided that the supercell is at least 12 Å. For large-scale calculations, where resources must be used most efficiently, it is likely that an even lower PW cutoff energy suffices.

Figure 6 shows the radial representation of the spin density in real space in the vicinity of the nucleus for different supercell sizes. The PW cutoff energy for the wave functions is 200 eV. The analytical data for atomic ^{7}Li were calculated using the ATOMDEF Package[58] with gradient-corrected exchange[36] and Vosko-Wilk-Nusair correlation[59] functionals. As could be expected from Fig. 4 the spin density near the nucleus is rather sensitive to the supercell size. The outer s-like wave function which is essential to properly describe

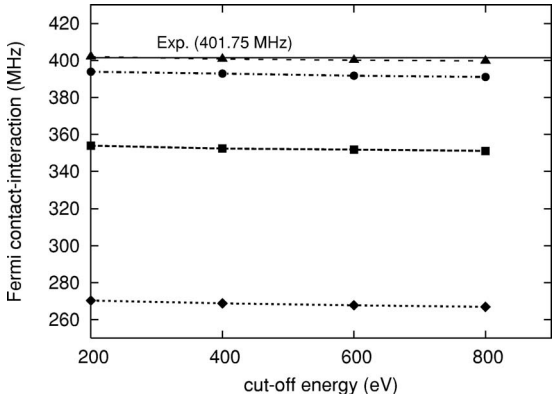

FIG. 5. Computed Fermi contact interaction for atomic ^{7}Li as a function of the cutoff energy of the wave-function plane-wave expansion, at supercell sizes of 6, 8, 10, and 12 Å (diamonds, squares, circles, and triangles). Lines are guides to the eye only. The experimental value (solid line) is from Ref. 57.

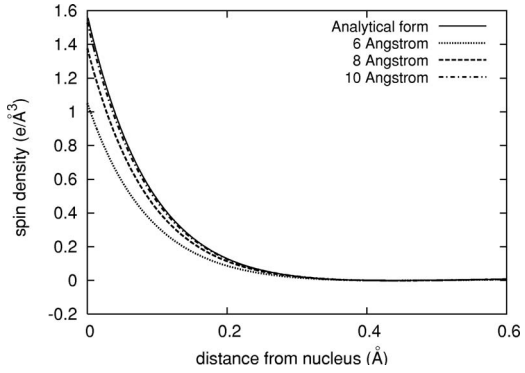

FIG. 6. Computed radial spin density of atomic ^{7}Li for various supercell sizes compared with analytic result (see text).

the Fermi contact interaction is spatially very extended. Therefore, in reciprocal space there must be a dense grid around the Γ point. However, in these calculations on finite systems we do not perform **k**-point sampling (Γ point only). Thus, such a dense grid can be obtained only if the real-space periodicity is sufficiently large. This also clarifies why the cutoff energy of the PW's for the wave-function expansion is not so important, because this does not refine the grid. Rather as this energy is increased, more distant points are added to the grid.

Below, we compare our results with other methods, some of which include relativistic effects. Relativistic effects can be separated into scalar relativistic (SR) and spin-orbit (SO) effects. It must be emphasized that in order to treat systems with heavier elements relativistic effects must be included in the calculations. A number of practical routes for relativistic calculations are available. Methods considered are either based on (1) approximate numerical solutions of the Dirac equation[60,61] or based on (2) different types of transformed-Hamiltonian methods such as zeroth-order-regular-approximation (ZORA),[62–64] infinite-order-regular-approximation with modified metric [IORA(mm)],[57] and Douglas-Kroll-Hess (DKH) methods.[13,65–69] Other computational details of comparative methods are as follows: in Refs. 63, 64, and 70, DFT calculations employed Becke exchange[71] and Perdew correlation[72] functionals (BP86). In other cases we have compared with results we obtained with the GAUSSIAN 98 package.[73]

IV. RESULTS AND DISCUSSION

A. Calculation results

As a first step to evaluate the efficiency of the MB method in comparison with other methods, the isotropic HFP's for group-II atomic ions $^{25}Mg^+$, $^{43}Ca^+$, and $^{87}Sr^+$ are examined. Table I summarizes isotropic HFP's from our MB method, the DKH method, and the four-component coupled-cluster (CC) method, as well as results from DFT GAUSSIAN 98 (Ref. 74) and experimental data. Reassuringly, the computationally most demanding CC results overall are closest to the experimental measurements. The table indicates that the MB results for $^{25}Mg^+$ and $^{43}Ca^+$ are in good agreement with experimental data, better than the DFT GAUSSIAN 98 (Ref. 74) results and the DK2+DK1 results, and about as good as the DK2+DK2 numbers. For $^{87}Sr^+$ our MB results are not as good as could be anticipated from our neglect of relativistic effects. The importance of relativistic effects is apparent from the large difference between the two implementations of the DKH, the DK2+DK1, and the DK2+DK2 methods.

The success of the MB method for $^{25}Mg^+$ and $^{43}Ca^+$ originates from the numerical AO's in the basis which are ideally suited to represent the *s* wave functions which are known to have a nonvanishing radial derivative at the nucleus. Therefore, generally, we may expect the MB method to be better suited than Gaussian basis functions for the calculation of isotropic HFP's.

In order to further test the MB method, it has been applied to three alkali-metal atoms (^{7}Li, ^{23}Na, and ^{39}K) and two transition-metal atoms (^{63}Cu and ^{107}Ag). Table II shows isotropic HFP's using the MB method and various other methods and as determined experimentally.

Table II shows that for all elements, except ^{107}Ag, the MB results agree well with experimental data. For ^{63}Cu the deviation from experiment is noticeable for methods which treat relativistic effects approximately, such as DKH, ZORA, and IORA(mm). As the DKH and ZORA methods should, in principle at least, be superior to the MB method, it suggests that the basis sets used in the former two methods cannot produce accurate enough wave functions for the *s* orbitals. Probably, one of the major challenges for the implementation of such transformed-Hamiltonian methods is that the operator responsible for the magnetic interaction should be transformed in the same way as that for the unperturbed Hamiltonian and for the wave function. The situation for ^{107}Ag is completely different; here, nonrelativistic results fail to reach

TABLE I. Comparison of isotropic HFP's (in MHz) for group-II cations.

Atom	MB[a]	DK2+DK1[b]	DK2+DK2[b]	GAUSSIAN 98[a]	CC[b]	Expt.[b]
$^{25}Mg^+$	−600.2	−560	−601	−598.5[c]	−593.7	±596.2
$^{43}Ca^+$	−812.8	−723	−813	−789.8[c]	−792.8	±806.4
$^{87}Sr^+$	−912.7	−883	−1061	−877.9[d]	−1000	990–1000.5

[a]Present work.
[b]Computed and experimental data from Ref. 70.
[c]DFT-B3LYP with 6-311+G(*d*) basis set.
[d]DFT-B3LYP with universal Gaussian basis set (UGBS) (Ref. 75).

TABLE II. Comparison of isotropic HFP's (in MHz) for alkali-metal atoms (^{7}Li, ^{23}Na, and ^{39}K) and transition-metal atoms (^{63}Cu and ^{107}Ag).

Atom	MB[a]	DK2+DK1[b]	DK2+DK2[b]	ZORA[c]	IORA(mm)[d]	GAUSSIAN 98[a]	Expt.[e]
^{7}Li	401.6	—	—	—	401.6	373.3[f]	401.7
^{23}Na	891.2	—	—	—	866.9	630.3[f]	885.8
^{39}K	232.4	—	—	—	226.1	152.8[f]	230.9
^{63}Cu	5935.1	5786	6726	6598	5411	−5646.5[f]	5867
^{107}Ag	−1411.3	−1613	−1965	−1862	−1698	−1253.4[g]	−1713

[a]Present work.
[b]DKH results from Ref. 70.
[c]ZORA results from Ref. 63.
[d]IORA(mm) results from Ref. 57.
[e]Experimental data of alkali-metal atoms (^{7}Li, ^{23}Na, and ^{39}K), ^{63}Cu, and ^{107}Ag from Refs. 76–78 respectively.
[f]DFT-B3LYP using 6-311G(*d*) basis set.
[g]DFT-B3PW91 using UGBS (Ref. 75).

reasonable agreement with experimental data as is to be expected on the basis of its atomic number.

As shown in Tables I and II, the MB values for $^{87}Sr^{+}$ and Ag are smaller than experiment. Additionally, comparing the MB results with the DKH2+DKH2, ZORA, and IORA(mm), we see that relativistic effects enhance HFP's appreciably for these two cases. This is due to the large relativistic contraction of the atomic *s*-electron density from which the isotropic HFP's are obtained. Thus, for a proper accounting of the relativistic effect for heavy atoms such as ^{87}Sr and ^{107}Ag, the basis set must be able to reproduce accurately the spin-dependent contraction of the *s* orbitals. Going beyond the point distribution of nuclear charge and nuclear dipole moment is another approach which has been argued to improve the agreement between calculated and measured isotropic HFP's. However, it appears mostly used to overcome singularities at the nucleus in the GGA.[14,15]

On the basis of Tables I and II it appears that for atomic numbers *Z* up to the low 30's the MB method can give good results for the isotropic HFP's.

The hyperfine properties of small molecules and clusters provide a more practically relevant test than atomic calculations. The results of zinc complexes ^{67}Zn*X* are indicated in Table III in order of increasing electronegativity of *X*: $^{107}Ag < {}^{1}H < {}^{13}CN < {}^{19}F$. ^{107}Ag has about the same electronegativity as ^{67}Zn. In the Zn*X* complexes a fully occupied bonding σ hybrid and a single occupied antibonding σ hybrid exist between the σ AO (or MO) of the *X* complex and the ^{67}Zn 4*s* AO.[64] Therefore, it is to be expected that with increasing electronegativity of *X* the bonding orbital becomes more like the σ AO (or MO) of *X* while the SOVO becomes more like the ^{67}Zn 4*s* state. In other words, the spin becomes more localized on zinc and the ^{67}Zn isotropic hyperfine interaction A_{iso} should increase. This trend, as shown by our method and relativistic methods, is similarly followed by the experimental values. In the view of very polar bonding in ZnF, it is likely that the matrix environment of the

TABLE III. HFP parameters (in MHz) for zinc complexes.

		Zn part		*X* part	
Complex (Zn*X*)	Method	A_{iso}	A_{aniso}	A_{iso}	A_{aniso}
$^{67}Zn^{107}Ag$	MB[a]	333.2	26.5	−1051.4	−0.1
	DK2+DK1[b]	320	22	−1140	1
	DK2+DK2[b]	373	23	−1401	0
	ZORA[c]	357	21	−1297	−1
	GAUSSIAN 98[e]	225.3	22.7	−962.2	1.6
	Expt.[c]	—	—	−1324	0
$^{67}Zn^{1}H$	MB[a]	549.2	74.1	468.5	−1.3
	DK2+DK1[b]	512	66	511	−1
	DK2+DK2[b]	597	65	512	−1
	ZORA[c]	561	63	543	0
	GAUSSIAN 98[d]	419.6	52.2	457.8	−2.94
	Expt.[c]	—	—	486	−2
$^{67}Zn^{13}CN$	MB[a]	980.1	64.4	258.4	23.1
	DK2+DK1[b]	948	55	348	38
	DK2+DK2[b]	1106	55	255	37
	ZORA[c]	1044	53	253	38
	GAUSSIAN 98[e]	997.6	49.4	261.2	27.8
	Expt.[c]	—	—	—	—
$^{67}Zn^{19}F$	MB[a]	1151.6	60.5	196.2	822.6
	DK2+DK1[b]	1109	41	228	862
	DK2+DK2[b]	1294	41	241	861
	ZORA[c]	1223	40	235	866
	GAUSSIAN 98[e]	1151.1	34.5	244.5	677.21
	Expt.[c]	—	—	129	816

[a]Present work.
[b]DKH results from Ref. 70.
[c]ZORA results and experimental data from Ref. 63.
[d]DFT-B3LYP using 6-311+G(*d*) basis set.
[e]DFT-B3PW91 using UGBS (Ref. 75).

TABLE IV. HFP parameters (in MHz) for the $^{63}Cu_7$ cluster.

Parameter	Method	^{63}Cu(2)	^{63}Cu(5)
A_{iso}	MB[a]	1750	−51
	Arratia-Perez[b]	1787	−53
	SR-ZORA[c]	—	—
	Empirical[d]	1747	54
$A_\perp$	MB[a]	1781	−51
	Arratia-Perez[e]	1839	40
	SR-ZORA[c]	1683	—
	Expt.[d]	1794	54
$A_\parallel$	MB[a]	1688	−51
	Arratia-Perez[e]	1783	40
	SR-ZORA[c]	1714	—
	Expt.[d]	1654	54

[a]Present work.
[b]Reference 79, with DFT-IV basis set.
[c]Reference 63, unrestricted SR-ZORA results.
[d]Reference 80, empirical and experimental results.
[e]Reference 79, with DSW-NR-I basis set.

complexes significantly affects the experimental determinations. Nevertheless, the overall agreement with experiment and other computations is reasonable, with the exception of ^{107}Ag as discussed previously on the basis of relativistic effects.

Finally, to test the accuracy of our method for clusters, the results for the $^{63}Cu_7$ cluster have been summarized in Table IV and contrasted with results in the literature. The point-group symmetry of $^{63}Cu_7$ was found to be D_{5h}, a pentagonal bipyramid as illustrated in Fig. 7. The five copper atoms on the pentagonal ring are referred to as ^{63}Cu(5), and the two axial copper atoms are labeled ^{63}Cu(2).

MB computations indicate that the spin density is mostly on the ^{63}Cu(2) atoms with only minor contributions at the ^{63}Cu(5) atoms as is evident from Fig. 8. Accordingly, the HFP's on the ^{63}Cu(2) sites are dominant. Anisotropy is absent on the ^{63}Cu(5) sites which is in accordance with an assumption made in experimental work, $A_\perp(5)=A_\parallel(5)=A_{iso}(5)$.[80] The anisotropy on the ^{63}Cu(2) sites is measured to be weak.[80] The ^{63}Cu(5) sites have negative HFP's. Since the g_j value for ^{63}Cu is positive,[81,82] this negative sign contribution, as shown in Table IV, indicates that the spin density near the ^{63}Cu(5) nuclei is of opposite sign as the spin polarization of the $^{63}Cu_7$ cluster. Relativistic effects are not significant as is clear from comparing nonrelativistic and relativistic results. Agreement with experiment is good and, in fact, a little better than obtained with other methods.

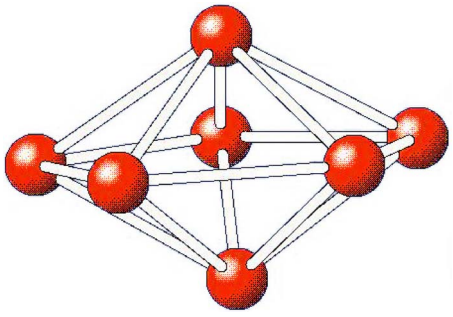

FIG. 7. (Color online) Bipyramid Cu_7 cluster.

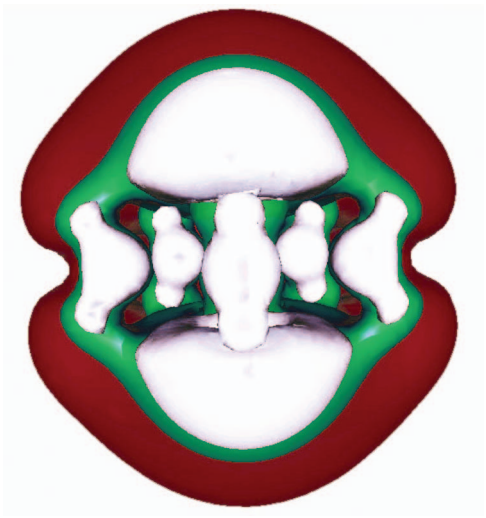

FIG. 8. (Color) Cu_7 spin density, isosurface coloration: white $\rho_s=0.01$ e/Å^3, green $\rho_s=0.005$ e/Å^3, and red $\rho_s=0.001$ e/Å^3.

B. Spin polarization of core shells

As derived in Sec. II J the spin polarization of the core levels comes about through the exchange interaction with the SOVO. It is this relation between SOVO type and spin polarization near the nucleus that makes hyperfine measurements so useful for analysis of bonding around a defect center. Figures 9 and 10 show radial distribution functions pertaining to the wave functions of the core s orbitals and the SOVO. It is important to point out that SOVO with $l\neq 0$ nevertheless strongly contribute to the perturbing potential with $l=0$, so that in the following we will use the word "overlap" freely and speak of overlap between an $l\neq 0$ SOVO and s core levels. For the Ca^+ ions there is little overlap between the 4s-like SOVO and core 1s, 2s, and 3s states while the Mn 3d-like SOVO strongly overlaps with the

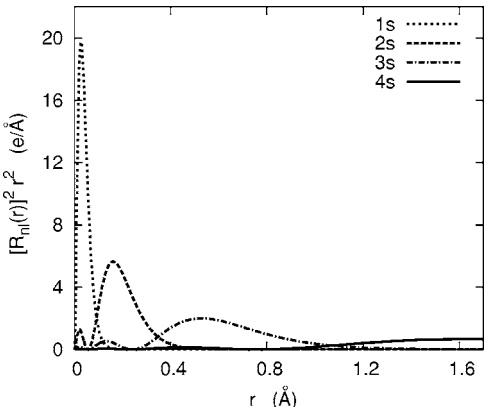

FIG. 9. Radial distribution functions $[R_{nl}(r)]^2r^2$ for Ca^+.

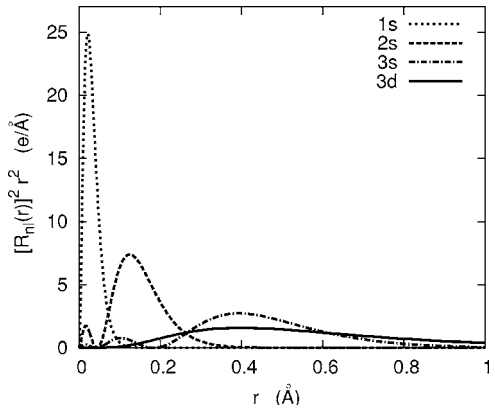

FIG. 10. Radial distribution functions $[R_{nl}(r)]^2 r^2$ for atomic Mn.

core $2s$ and $3s$ states. For systems with little overlap between SOVO and core levels (see Fig. 9), as discussed, little spin polarization of core levels is to be expected. As illustrated in Table V, for atoms and cations with s-like SOVO, the contribution of core shells to the total spin density at the metal nucleus is small, less than 1.7% of the total spin density. In contrast, for systems with large overlap between SOVO and core levels (see Fig. 10), spin polarization of core levels plays a role. Table V shows that for transition metals with mostly d-like SOVO, such as Cr^+, Mn^{2+}, and Fe^{3+}, core contributions to the nucleus spin density are dominant. The sequence Mn, Mn^+, and Mn^{2+} illustrates the effect of the $4s$ states near the nucleus: in Mn (atomic case) there are two $4s$ electrons so that the contribution to the spin density at the nucleus derives from the deformation of the $4s_\uparrow$ and $4s_\downarrow$ states; in Mn^+, only the majority $4s_\uparrow$ state is occupied, making for a huge spin density, while in Mn^{2+} the $4s$ states are unoccupied.

Energetically, the splitting of core levels caused by the exchange interaction with the SOVO was found to be negligible (K and Ca^+) or small (Cu) for metals with $4s$-type SOVO. It becomes significant for transition metals with d-like SOVO. Table VI shows the multiplet splitting between $ns_\uparrow$ and $ns_\downarrow$ states, as obtained from Eq. (108) and as obtained directly from the Kohn-Sham (KS) DFT calculations. The good agreement between $\Delta\tilde{\varepsilon}^\lambda_\uparrow - \Delta\tilde{\varepsilon}^\lambda_\downarrow$ from Eq. (108) and from direct KS calculations implies that the first-order perturbation treatment is adequate for the analysis of core spin polarization. In all cases, the $1s$ shift seems to be negligible, confirming that the exchange interaction between SOVO and $1s$ is small. A similarly weak splitting occurs for the $2s$ levels in the $4s$-type SOVO atoms. In contrast, the splitting of $2s$ and $3s$ levels is significant for transition metals with $3d$-like SOVO. Figure 11 shows that the perturbing effective potential is proportional to the charge state (and the local moment) for ions with a charge 2+ or higher. For Mn and Mn^+ $4s$ electrons come into play also. This proportionality is easily recognized for the $3s$ levels in Table VI. It is apparent that the local magnetic moment of the $3d$-type ion plays a larger role than the specific element as the differences between say Mn^{6+} and Fe^{7+} are small as has been found in experiment also; see, e.g., Fig. 8 in Ref. 86. The computed multiplet splittings generally appear to agree with experimental results, (for Mn and Mn^{2+}, see Fig. 10 of Ref. 87; for Fe, see Refs. 86 and 88–90). The general agreement with experiment might make Eq. (108) of utility for the analysis of non-s-like semicore levels as well.[91–93] Of course, the actual complicated peak shapes require a more sophisticated treatment.[90]

1. Analysis of core-level spin polarization for 3d-type SOVO

Mn is used as an example of the group of transition metals characterized by unpaired electrons in the $3d$ shell. To

TABLE V. Spin densities at the metal nuclei $\rho_s(\mathbf{R})$ (in $e/\text{Å}^3$) for $4s$-type SOVO, K, Ca^+, and Cu, and $3d$-type SOVO, Cr^+, Mn, Mn^+, Mn^{2+}, and Fe^{3+}. The experimental values of ^{39}K, $^{43}Ca^+$, and ^{63}Cu were taken from their corresponding isotropic HFP's using Eq. (85) with g and μ values from Ref. 48. VS refers to valence shells other than the SOVO.

	Core shells			Valence shells			
Atom	$1s$	$2s$	$3s$	VS	SOVO	Total	Expt.
K	0.02	−0.03	−0.08	0.00	7.40	7.31	7.46[a]
Ca^+	0.06	−0.07	−0.16	0.00	18.38	18.23	18.16[b]
Cu	0.05	−0.15	−0.35	0.00	34.04	33.59	33.58[c]
Cr^+	−0.01	−7.80	2.08	0.00	0.00	−5.73	—
Mn	−0.01	−8.42	4.34	2.14	0.00	−1.95	−2.02[d]
Mn^+	0.09	−9.62	3.60	0.00	29.32	23.39	23.82[e]
Mn^{2+}	−0.01	−10.02	3.95	0.00	0.00	−6.08	−6.19[e]
Fe^{3+}	−0.01	−12.95	6.98	0.00	0.00	−5.98	−4.68⋯−6.07[f]

[a]From Ref. 76.
[b]From Ref. 63.
[c]From Ref. 77.
[d]From Ref. 83.
[e]From Ref. 84.
[f]From Ref. 85.

TABLE VI. Multiplet splitting (in eV) of s-type (semi)core levels, as calculated from Eq. (108) and as obtained directly from Kohn-Sham DFT calculations (KS) for 4s-type SOVO, K, Ca^+, and Cu and 3d-type SOVO, Mn ions, and Fe ions, and magnetic moment (m) in Bohr magnetons.

		Eq. (108)			KS		
Atom	$m(\mu_B)$	1s	2s	3s	1s	2s	3s
K	1	−0.01	−0.01	−0.03	−0.01	−0.02	−0.03
Ca^+	1	−0.03	−0.03	−0.07	−0.03	−0.03	−0.06
Cu	1	−0.02	−0.20	−0.48	−0.02	−0.23	−0.42
Mn	5	−0.04	−2.30	−4.82	−0.05	−2.26	−4.20
Mn^+	6	−0.07	−2.29	−5.28	−0.09	−2.30	−4.91
Mn^{2+}	5	−0.04	−2.30	−5.30	−0.04	−2.32	−4.93
Mn^{3+}	4	−0.03	−2.10	−4.61	−0.04	−2.12	−4.38
Mn^{4+}	3	−0.03	−1.80	−3.84	−0.04	−1.81	−3.60
Mn^{5+}	2	−0.02	−1.31	−2.77	−0.03	−1.37	−2.62
Mn^{6+}	1	−0.01	−0.62	−1.49	−0.02	−0.67	−1.43
Fe	4	−0.04	−2.52	−4.07	−0.05	−2.52	−3.97
Fe^+	5	−0.05	−2.82	−5.94	−0.06	−2.85	−5.59
Fe^{2+}	6	−0.10	−2.82	−5.96	−0.13	−2.86	−5.61
Fe^{3+}	5	−0.05	−2.82	−5.93	−0.06	−2.86	−5.59
Fe^{4+}	4	−0.04	−2.53	−5.15	−0.06	−2.57	−4.86
Fe^{5+}	3	−0.03	−2.12	−4.16	−0.05	−2.15	−3.95
Fe^{6+}	2	−0.02	−1.57	−2.98	−0.04	−1.60	−2.85
Fe^{7+}	1	−0.01	−0.78	−1.59	−0.02	−0.81	−1.55

illustrate our discussion we show, in Fig. 12(a), $\Delta V_\uparrow(r)$ along with a few selected $F^{\lambda\kappa}$ which contribute significantly to the $C^{\lambda\kappa}$, while in Fig. 12(b) their product $\Delta V_\uparrow^{\lambda\kappa}$ [Eq. (106)] is shown. $\Delta V_\uparrow(r)$ is localized near the core region, as is to be expected on the basis of Eq. (105), so that the core levels overlap with it.

As the 1s level is so strongly localized near the nucleus, only F^{1s2s} overlaps with $\Delta V_\uparrow(r)$. $\Delta V_\uparrow^{1s2s}$ shows a positive peak so that, according to Eq. (95) C^{1s2s} is negative, but of small magnitude. Therefore Ψ^{1s} is weakly spin polarized with opposite sign as the global spin polarization.

For $\lambda=2s$, in addition to F^{1s2s} which was considered above, the negative parts of F^{2s3s} and to a lesser extent F^{2s4s}

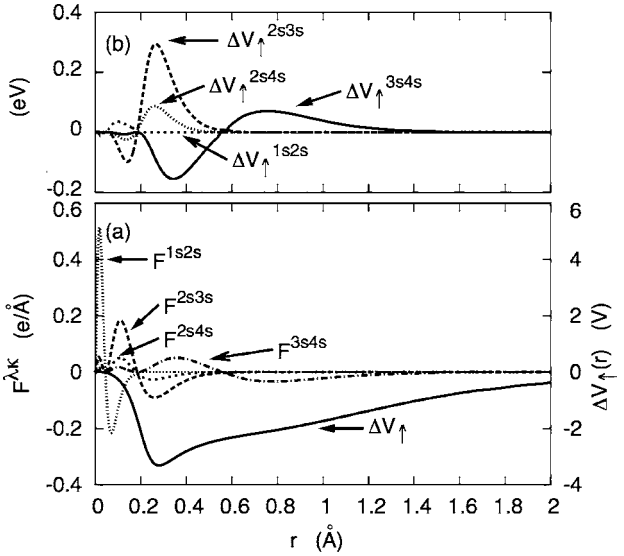

FIG. 12. Contributions to $C^{\lambda\kappa}$: (a) $\Delta V_\uparrow(r)$ and $F^{\lambda\kappa}$ and in (b) their product $\Delta V_\uparrow^{\lambda\kappa}$ for Mn.

overlap with $\Delta V_\uparrow(r)$. The radial integral over $\Delta V_\uparrow^{2s3s}$ and $\Delta V_\uparrow^{2s4s}$ is positive, so that C^{2s3s} and C^{2s4s} are negative. Thus, the spin-polarized $\tilde{\Psi}_\uparrow^{2s}$ can be expressed as

$$\tilde{\Psi}_\uparrow^{2s} \simeq |C^{2s1s}|\Psi^{1s} + \Psi^{2s} - |C^{2s3s}|\Psi^{3s} - |C^{2s4s}|\Psi^{4s}, \tag{109}$$

where

$$|C^{2s1s}| < |C^{2s4s}| < |C^{2s3s}|. \tag{110}$$

It follows that the 2s core level is significantly spin polarized with opposite sign as the global spin polarization. For $\lambda=3s$, F^{2s3s} and F^{3s4s} have dominant overlap with $\Delta V_\uparrow(r)$. However, the radial integrand of $\Delta V_\uparrow^{3s4s}$, albeit positive, almost vanishes. Thus,

$$\tilde{\Psi}_\uparrow^{3s} \simeq |C^{3s2s}|\Psi^{2s} + \Psi^{3s} - |C^{3s4s}|\Psi^{4s}, \tag{111}$$

where

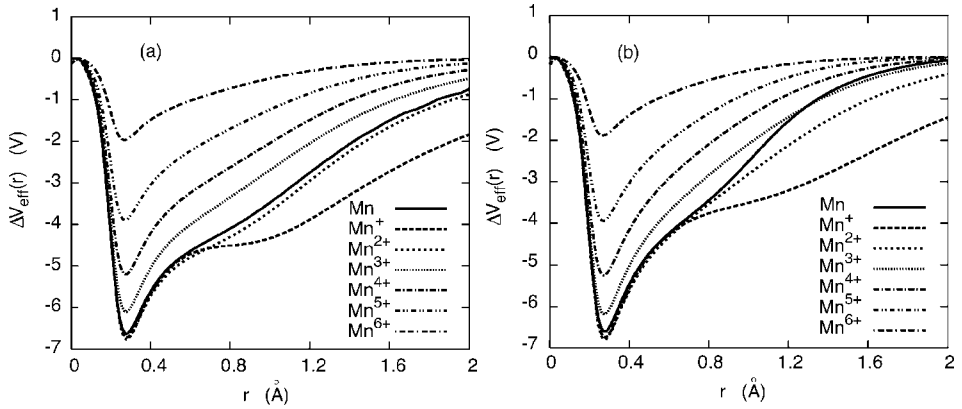

FIG. 11. $\Delta V_{eff}(r)$ for atomic Mn and its ions as obtained from (a) Eq. (105) and as obtained directly from (b) Kohn-Sham DFT calculations (KS).

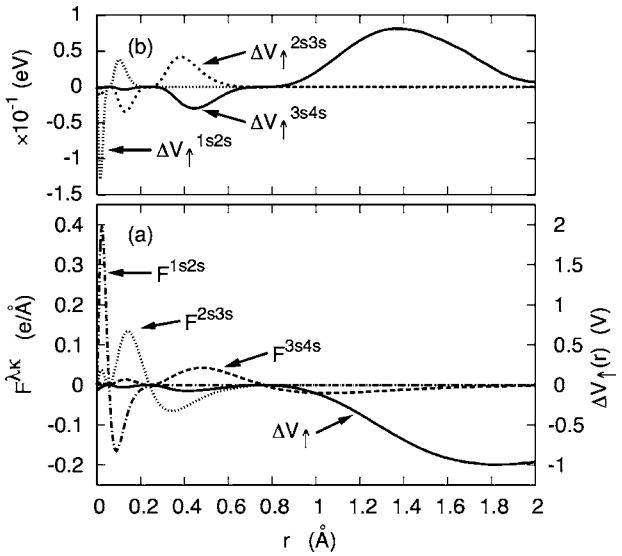

FIG. 13. Contributions to $C^{\lambda\kappa}$: (a) $\Delta V_{\uparrow}(r)$ and $F^{\lambda\kappa}$ and in (b) their product $\Delta V_{\uparrow}^{\lambda\kappa}$ for Ca^{+}.

$$|C^{3s4s}| < |C^{3s2s}| \tag{112}$$

and the 3*s* core level is oppositely spin polarized as the 2*s* core level—i.e., with the same sign as the global spin polarization.

The results of our MB calculations show a similar pattern of core spin polarization among other ionic and atomic transition metal systems. According to Table V the 2*s*-level contribution to the spin density at the nucleus point is negative while that of the 3*s* level is positive. In Table V one outlier is seen: for Mn^{+} the 4*s* level contributes to the SOVO which completely dominates the spin density at the nucleus.

2. Analysis of core-level spin polarization for 3d–type SOVO

The Ca^{+} ion has one unpaired electron in its 4*s* level. A characteristic of the 4*s*-type SOVO is that it is much outward expanded and the exchange interaction with core shells is very weak. This is readily apparent from Eq. (105) and Fig. 3. Moreover, as ρ^{SOVO} does not vanish at the nucleus, $\Delta V_{\uparrow}$ is non-vanishing near the nucleus.

$\Delta V_{\uparrow}(r)$ along with significant $F^{\lambda\kappa}$ are displayed in Fig. 13(a) and their product $\Delta V_{\uparrow}^{\lambda\kappa}$ in Fig. 12(b).

For the highly localized $\lambda=1s$ level, since $\Delta V_{\uparrow}(r)$ does not vanish at the nucleus, the positive part of F^{1s2s} overlaps with $\Delta V_{\uparrow}(r)$ most, so that $\Delta V_{\uparrow}^{1s2s}$ becomes negative [Fig. 13(b)] and C^{1s2s} takes a positive value. The spin-polarized 1*s* level contributes positively to the spin density at the nucleus. For $\lambda=2s$, F^{2s3s} also has significant overlap with $\Delta V_{\uparrow}$ leading to a positive $\Delta V_{\uparrow}^{2s3s}$, giving a negative C^{2s3s}. As C^{2s3s} and C^{2s1s} are both negative, the 2*s* level contributes negatively to the spin density at the nucleus. In the case of $\lambda=3s$ the negative part of F^{3s4s} occurs towards the negative peak of $\Delta V_{\uparrow}(r)$. Therefore, as illustrated in Fig. 13(b), $\Delta V_{\uparrow}^{3s4s}$ is strongly positive so that C^{3s4s} is negative. C^{3s2s} is positive, but of much smaller magnitude than C^{3s4s} and therefore the 3*s* level contributes negatively to the spin density at the nucleus. Similar patterns of core spin polarization have been found for K and Cu; see Table V. For K, Ca^{+}, and Cu the 3*s* orbital gives the largest spin density at the nucleus, but in all cases opposing the global spin polarization.

V. CONCLUSIONS

An all-electron full-potential density functional electronic structure method, the so-called mixed-basis method, has been presented which allows hyperfine parameters to be calculated for ions, atoms, molecular complexes, and clusters. While earlier work showed the method to give geometries in agreement with other highly accurate all-electron methods, here we show that the method is especially well suited for the calculation of hyperfine parameters. The fact that the one-electron wave functions are expanded in terms of plane waves and localized atomic orbitals is very advantageous for an accurate representation of the spin density near the atomic nuclei. As a consequence, the mixed-basis method typically achieves better agreement on the hyperfine parameters than other density functional methods with less optimal expansions for the one-electron wave functions. The radial representation of effective potentials and charge densities makes it a convenient method to analyze the various contributions to the spin polarization in the neighborhood of the nucleus. Our neglect of relativistic effects currently limits us to the lighter elements, typically for atomic numbers up to the low 30's. Through a LSDA-based derivation of the exchange-induced perturbing potential, the core-level contribution to the spin polarization near the nucleus and the contribution to the isotropic hyperfine parameters was analyzed in detail.

ACKNOWLEDGMENTS

This work was performed under the interuniversity cooperative research program of the Laboratory for Advanced Materials, Institute for Materials Research, Tohoku University. The authors gratefully acknowledge the Center for Computational Materials Science at the Institute for Materials Research for allocations on the Hitachi SR8000 supercomputer system. M.S. gratefully acknowledges Professor K. Ohno of the National University of Yokohama for an earlier version of the mixed-basis program and for many instructive discussions.

*Current address: Department of Material Science & Engineering, Delft University of Technology, 2628AL Delft, The Netherlands.

[1] N. T. Son, E. Janzén, J. Isoya, and S. Yamasaki, Phys. Rev. B **70**, 193207 (2004).

[2] R. L. Lichti, W. A. Nussbaum, and K. H. Chow, Phys. Rev. B **70**, 165204 (2004).

[3] V. Bellini, S. Cottenier, M. Cakmak, F. Manghi, and M. Rots, Phys. Rev. B **70**, 155419 (2004).

[4] T. Graf, T. Ishikawa, K. M. Itoh, E. E. Haller, M. Stutzmann, and M. S. Brandt, Phys. Rev. B **68**, 205208 (2003).

[5] Ph. Mavropoulos, N. Stefanou, B. Nonas, R. Zeller, and P. H. Dederichs, Phys. Rev. Lett. **81**, 1505 (1998).
[6] S. Ögüt and J. R. Chelikowsky, Phys. Rev. Lett. **91**, 235503 (2003).
[7] Y. Furukawa, S. Kawakami, K. Kumagai, S.-H. Baek, and F. Borsa, Phys. Rev. B **68**, 180405(R) (2003).
[8] S. I. Erlingsson and Y. V. Nazarov, Phys. Rev. B **70**, 205327 (2004).
[9] M. Fujii, A. Mimura, S. Hayashi, Y. Yamamoto, and K. Murakami, Phys. Rev. Lett. **89**, 206805 (2002).
[10] A. Derevianko and S. G. Porsev, Phys. Rev. A **71**, 032509 (2005).
[11] T. Nagasawa, A. Haga, and M. Nakano, Phys. Rev. C **69**, 034322 (2004).
[12] F. Stevens, H. Vrielinck, F. Callens, E. Pauwels, and M. Waroquier, Phys. Rev. B **66**, 134103 (2002).
[13] B. A. Hess, Phys. Rev. A **33**, 3742 (1986).
[14] M. Battocletti, H. Ebert, and H. Akai, Phys. Rev. B **53**, 9776 (1996).
[15] R. H. Luchsinger, Y. Zhou, and P. F. Meier, Phys. Rev. B **55**, 6927 (1997).
[16] P. Novák, J. Kunes, W. E. Pickett, W. Ku, and F. R. Wagner, Phys. Rev. B **67**, 140403(R) (2003).
[17] R. J. Harrison and N. C. Handy, Chem. Phys. Lett. **98**, 97 (1983).
[18] R. J. Gdanitz, Chem. Phys. Lett. **312**, 578 (1999).
[19] O. V. Yazyev, I. Tavernelli, L. Helm, and U. Röthlisberger, Phys. Rev. B **71**, 115110 (2005).
[20] C. G. Van de Walle and P. E. Blöchl, Phys. Rev. B **47**, 4244 (1993).
[21] K. Ohno, K. Esfarjani, and Y. Kawazoe, *Computational Materials Science*, Solid State Sciences Series, Vol. 129 (Springer Verlag, Berlin, 1999).
[22] K.-M. Ho, C. Elsässer, C. T. Chan, and M. Fähnle, J. Phys.: Condens. Matter **4**, 5189 (1992).
[23] K.-M. Ho, C. Elsässer, C. T. Chan, and M. Fähnle, J. Phys.: Condens. Matter **4**, 5207 (1992).
[24] T. Korhonen, A. Settels, N. Papanikolaou, R. Zeller, and P. H. Dederichs, Phys. Rev. B **62**, 452 (2000).
[25] S. G. Louie, K.-M. Ho, and M. L. Cohen, Phys. Rev. B **19**, 1774 (1979).
[26] K.-M. Ho, C.-L. Fu, and B. N. Harmon, Phys. Rev. B **28**, 6687 (1983).
[27] C. Elsässer, N. Takeuchi, K.-M. Ho, C. T. Chan, P. Braun, and M. Fähnle, J. Phys.: Condens. Matter **2**, 4371 (1990).
[28] W. Kohn and L. J. Sham, Phys. Rev. **140**, A1133 (1965).
[29] A. Canning, W. Mannstadt, and A. J. Freeman, Comput. Phys. Commun. **130**, 233 (2000).
[30] For other versions of the multiplicative approach see, e.g., Eq. (6) in Ref. 27 and Sec. 2.2 of H. G. Bekker, PhD. Thesis, Dept. of Applied Physics, Univ. Twente, Enschede, The Netherlands, 1997.
[31] P. Hohenberg and W. Kohn, Phys. Rev. **136**, B864 (1964).
[32] R. O. Jones and O. Gunnarsson, Rev. Mod. Phys. **61**, 689–746 (1989).
[33] E. U. Condon and G. H. Shortley, *The Theory of Atomic Spectra* (Cambridge University Press, Cambridge, England, 1951).
[34] M. Tinkham, *Group Theory and Quantum Mechanics* (McGraw-Hill, New York, 1964).
[35] M. Weissbluth, *Atoms and Molecules* (Academic, New York, 1978), p. 12.
[36] J. P. Perdew, K. Burke, and M. Ernzerhof, Phys. Rev. Lett. **77**, 3865 (1996).
[37] J. A. White and D. M. Bird, Phys. Rev. B **50**, R4954 (1994).
[38] J. P. Perdew and A. Zunger, Phys. Rev. B **B23**, 5048 (1981).
[39] B. Kohler, S. Wilke, M. Scheffler, R. Kouba, and C. Ambrosch-Draxl, Comput. Phys. Commun. **94**, 31 (1996).
[40] M. J. Gillan, J. Phys.: Condens. Matter **1**, 689 (1989).
[41] M. Weinert and J. W. Davenport, Phys. Rev. B **45**, 13709 (1992).
[42] R. Yu, D. Singh, and H. Krakauer, Phys. Rev. B **43**, 6411 (1991).
[43] H. B. Callen, *Thermodynamics and an Introduction to Thermostatistics* (Wiley, New York, 1985).
[44] P. Bendt and A. Zunger, Phys. Rev. Lett. **50**, 1684 (1983).
[45] C. Satoko, Chem. Phys. Lett. **83**, 111 (1981).
[46] C. Satoko, Phys. Rev. B **30**, 1754 (1984).
[47] M. Scheffler, J. P. Vigneron, and G. B. Bachelet, Phys. Rev. B **31**, 6541 (1985).
[48] D. R. Lide, *Handbook of Chemistry and Physics*, 85th ed. (CRC Press, Boca Raton, 2004), pp. 9–93.
[49] S. Blügel, H. Akai, R. Zeller, and P. H. Dederichs, Phys. Rev. B **35**, 3271 (1987).
[50] M. Richter, *Electronic Structure and Magnetism of Lanthanide, Actinide, and Transition Metal Systems* (Technischen Universität, Dresden, 1997).
[51] S. S. Hana, J. Heberle, G. J. Perlow, R. S. Perston, and D. H. Vincent, Phys. Rev. Lett. **4**, 513 (1960).
[52] D. A. Goodings and V. Heine, Phys. Rev. Lett. **5**, 370 (1960).
[53] U. von Barth and L. Hedin, J. Phys. C **5** 1629 (1972).
[54] G. L. Oliver and J. P. Perdew, Phys. Rev. A **20**, 397 (1979).
[55] J. C. Slater, *The Self-consistent Field for Molecules and Solids*, *Quantum Theory of Molecules and Solids*, Vol. 4 (McGraw-Hill, New York, 1974).
[56] R. Gáspár, Acta Phys. Acad. Sci. Hung. **3**, 263 (1954).
[57] M. Filatov and D. Cremer, J. Chem. Phys. **121**, 5618 (2004).
[58] R. Pis Diez, computer code ATOMDEF, version 1.4, 2003; can be downloaded from http://www.quimica.unlp.edu.ar/cequinor/rpd_en.htm
[59] S. H. Vosko, L. Wilk, and M. Nusair, Can. J. Phys. **58**, 1200 (1980).
[60] L. Visscher, Th. Enevoldsen, T. Saue, H. J. Aa. Jensen, and J. Oddershede, J. Comput. Chem. **20**, 1262 (1999).
[61] H. M. Quieney and P. Belanzoni, Chem. Phys. Lett. **353**, 253 (2002).
[62] S. K. Wolff and T. Ziegler, J. Chem. Phys. **110**, 7689 (1999).
[63] E. van Lenthe, A. van der Avoird, and P. E. S. Wormer, J. Chem. Phys. **108**, 4783 (1998).
[64] P. Belanzoni, E. van Lenthe, and E. J. Baerends, J. Chem. Phys. **114**, 4421 (2001).
[65] M. Pernpointner, M. Seth, and P. Schwerdtfeger, J. Chem. Phys. **108**, 6722 (1998).
[66] V. Kellö and A. J. Sadlej, Int. J. Quantum Chem. **68**, 159 (1998).
[67] I. Malkin, O. L. Malkina, and V. G. Malkin, Chem. Phys. Lett. **361**, 231 (2002).
[68] K. M. Neyman, D. I. Ganyushin, A. V. Matveev, and V. A. Nasluzov, J. Phys. Chem. **106**, 5022 (2002).
[69] R. Fukuda, M. Hada, and H. Nakatsuji, J. Chem. Phys. **118**, 1027 (2003).
[70] I. Malkin, O. L. Malkin, V. G. Malkin, and M. Kaupp, Chem. Phys. Lett. **396**, 268 (2004).
[71] A. D. Becke, Phys. Rev. A **38**, 3098 (1988).
[72] J. P. Perdew and Y. Wang, Phys. Rev. B **33**, R8800 (1986).

[73] M. J. Frisch *et al.*, computer code GAUSSIAN 98, revision A.9, Gaussian, Inc., Pittsburgh, PA, 1998.
[74] GAUSSIAN 98 calculations of $^{25}Mg^{+}$, $^{43}Ca^{+}$, and $^{87}Sr^{+}$ assumed a triplet for the spin multiplicity.
[75] E. V. R. de Castro and F. E. Jorge, J. Chem. Phys. **108**, 5225 (1998).
[76] G. H. Fuller and V. W. Cohen, Nucl. Data, Sect. A **5**, 433 (1969).
[77] Y. Ting and H. Lew, Phys. Rev. **105**, 581 (1957).
[78] G. Wessel and H. Lew, Phys. Rev. **92**, 641 (1953).
[79] R. Arratia-Perez, L. Alvarez-Thon, and P. Fuentealba, Chem. Phys. Lett. **397**, 408 (2004).
[80] R. J. Van Zee and W. Weltner, Jr., J. Chem. Phys. **92**, 6976 (1990).
[81] W. Weltner, Jr., *Magnetic Atoms and Molecules* (Dover, New York, 1989).
[82] J. R. Morton and K. F. Preston, J. Magn. Reson. (1969-1992) **30**, 577 (1978).
[83] P. H. Kasai, Acc. Chem. Res. **4**, 329 (1971).
[84] M. L. Munzarová and M. Kaupp, J. Phys. Chem. A **103**, 9966 (1999).
[85] A. Abragam and B. Bleaney, *Electron Paramagnetic Resonance of Transition Ions* (Clarendon Press, Oxford, 1970).
[86] L. E. Klebanoff, J. Vac. Sci. Technol. B **14**, 3140 (1996).
[87] J. F. Moulder, W. F. Stickle, P. E. Sobol, and K. D. Bomben, *Handbook of X-ray Photoelectron Spectroscopy* (Perkin-Elmer Corp., Eden Prairie, MN, 1992).
[88] F. U. Hillebrecht, T. Kinoshita, Ch. Roth, H. B. Rose, and E. Kisker, J. Magn. Magn. Mater. **212**, 201 (2000).
[89] D. J. Huang, W. P. Wu, J. Chen, C. F. Chang, S. C. Chung, M. Yuri, H.-J. Lin, P. D. Johnson, and C. T. Chen, Rev. Sci. Instrum. **73**, 3778 (2002).
[90] K.-H. Park, S.-J. Oh, K. Shimada, A. Kamata, K. Ono, A. Kakizaki, and T. Ishii, Phys. Rev. B **53**, 5633 (1996).
[91] A. Goldoni, A. Baraldi, G. Comelli, S. Lizzit, and G. Paolucci, Phys. Rev. Lett. **82**, 3156 (1999).
[92] P. G. Steeneken, L. H. Tjeng, I. Elfimov, G. A. Sawatzky, G. Ghiringhelli, N. B. Brookes, and D.-J. Huang, Phys. Rev. Lett. **88**, 047201 (2002).
[93] J. Henk and A. Ernst, J. Electron Spectrosc. Relat. Phenom. **125**, 107 (2002).